Predictive Models and Novel Accelerated Tests for the Reliability of Cell Metallization in Photovoltaic Modules

Cooperative Research and Development Final Report

CRADA Number: CRD-16-00603

NREL Technical Contact: Michael Kempe

NREL is a national laboratory of the U.S. Department of Energy
Office of Energy Efficiency & Renewable Energy
Operated by the Alliance for Sustainable Energy, LLC

This report is available at no cost from the National Renewable Energy Laboratory (NREL) at www.nrel.gov/publications.

Contract No. DE-AC36-08GO28308

Technical Report
NREL/TP-5K00-89243
March 2024

Predictive Models and Novel Accelerated Tests for the Reliability of Cell Metallization in Photovoltaic Modules

Cooperative Research and Development Final Report

CRADA Number: CRD-16-00603

NREL Technical Contact: Michael Kempe

Suggested Citation
Kempe, Michael. 2024. *Predictive Models and Novel Accelerated Tests for the Reliability of Cell Metallization in Photovoltaic Modules: Cooperative Research and Development Final Report, CRADA Number CRD-16-00603.* Golden, CO: National Renewable Energy Laboratory. NREL/TP-5K00-89243. https://www.nrel.gov/docs/fy24osti/89243.pdf.

NREL is a national laboratory of the U.S. Department of Energy
Office of Energy Efficiency & Renewable Energy
Operated by the Alliance for Sustainable Energy, LLC

This report is available at no cost from the National Renewable Energy Laboratory (NREL) at www.nrel.gov/publications.

Contract No. DE-AC36-08GO28308

Technical Report
NREL/TP-5K00-89243
March 2024

National Renewable Energy Laboratory
15013 Denver West Parkway
Golden, CO 80401
303-275-3000 • www.nrel.gov

NOTICE

This work was authored by the National Renewable Energy Laboratory, operated by Alliance for Sustainable Energy, LLC, for the U.S. Department of Energy (DOE) under Contract No. DE-AC36-08GO28308. Funding provided by U.S. Department of Energy Office of Energy Efficiency and Renewable Energy Solar Energy Technologies Office. The views expressed herein do not necessarily represent the views of the DOE or the U.S. Government.

This report is available at no cost from the National Renewable Energy Laboratory (NREL) at www.nrel.gov/publications.

U.S. Department of Energy (DOE) reports produced after 1991 and a growing number of pre-1991 documents are available free via www.OSTI.gov.

Cover Photos by Dennis Schroeder: (clockwise, left to right) NREL 51934, NREL 45897, NREL 42160, NREL 45891, NREL 48097, NREL 46526.

NREL prints on paper that contains recycled content.

Cooperative Research and Development Final Report

Report Date: March 1, 2024

In accordance with requirements set forth in the terms of the CRADA agreement, this document is the CRADA final report, including a list of subject inventions, to be forwarded to the DOE Office of Scientific and Technical Information as part of the commitment to the public to demonstrate results of federally funded research.

Parties to the Agreement: SunPower Corporation

CRADA Number: CRD-16-00603

CRADA Title: Predictive Models and Novel Accelerated Tests for the Reliability of Cell Metallization in Photovoltaic Modules

Responsible Technical Contact at Alliance/National Renewable Energy Laboratory (NREL):

Michael Kempe | Michael.Kempe@nrel.gov

Other Co-Authors or Contributors:

Peter Hacke | Peter.Hacke@nrel.gov

Joshua Morse | jbmorse8@gmail.com

Name and Email Address of POC at Company:

Katherine Han | katherine.han@maxeon.com

Darcy Osborne | darcy.osborne@sunpower.com

Other Co-Authors or Contributors:

Yu-Chen Shen | YuChenShen@gmail.com

Jichao Li | LiJichaocn@gmail.com

Sponsoring DOE Program Office(s):

Office of Energy Efficiency and Renewable Energy (EERE), Solar Energy Technologies Office (SETO)

Joint Work Statement Funding Table showing DOE commitment:

No NREL Shared Resources.

Estimated Costs	NREL Shared Resources a/k/a Government In-Kind
Original Agreement	$0.00
Modification #1	$0.00
Modification #2	$0.00
Modification #3	$0.00
TOTALS	$0.00

Executive Summary of CRADA Work:

Studies of metallization corrosion m photovoltaics have mainly been limited to comparisons of modules placed in accelerated chambers to fielded modules [1]. Damp Heat accelerated tests and phenomenological equations [2] are used to assess metallization corrosion without understanding the effect of UV light and temperature and humidity cycles on encapsulant adhesion degradation. The roles of encapsulant in-and out--diffusions of moisture and encapsulant impurities are important. Furthermore, few photovoltaic metallization corrosion studies included the role of bias and leakage currents, which are crucial in the electrochemical reaction of metallization. Leakage currents can highly accelerate the corrosion mechanism and are important to include in the studies of corrosion.

In our research plan, we will address the following gaps in the PV community's understanding of metallization corrosion: (1) metallization corrosion with bias, humidity, and impurities in the encapsulant or metallization; (2) humidity diffusion through fresh and degraded encapsulants; and (3) comparison of model predictions with outdoor field modules and SunPower's extensive data for its back-contact and front-contact fleets [2] along with NREL's store of >20 year old modules. Our goal is to build models and accelerated tests to predict long term degradation of metallization corrosion of photovoltaic modules in the field. Our studies will include metals used in c-Si solar cells (Cu, Ag, and Al) and commonly used encapsulants (EV A (ethylene vinyl acetate), TPO (thermoplastic olefin), and silicone).

CRADA benefit to DOE, Participant, and US Taxpayer:

Assists laboratory in achieving programmatic scope.

Summary of Research Results:

TASK DESCRIPTIONS:

Purpose:

In our proposed research, we plan to look at metallization interconnect reliability: metallization corrosion failures. The key outcomes of this research will be a) predictive models for metallization corrosion to aid in the design of reliable interconnects, b) predictive and faster accelerated tests useful for qualification, certification, and ongoing reliability. Success in the proposed research will be measured by how closely the predictions from the model and the new accelerated tests compare with outdoor field data.

Statement of Work

Technical Scope Summary of Metallization Corrosion.

In the first budget period, all outdoor exposures will be deployed, and the experimental materials and sample structures will be determined and constructed. The ranges of the main factors (RH: relative humidity, T: temperature, I: 1eadeakage currents, and impurities) will be determined, and exposure and monitoring of corrosion will begin. We will also do initial measurements of samples, which will be repeated during sample exposure.

In the second budget period, the corrosion mechanisms and the environmental parameters that affect metallization corrosion will be determined through ongoing testing and exposure. The corrosion rates will then be input into a lifetime PY model and compared to outdoor data.

In the third budget period, the model predictions will be compared to the metallization corrosion found in the fielded modules. Once the model is confirmed, an accelerated test will be developed. The predictions from the accelerated test will also be compared to field degradation. The metallization corrosion studies will encompass common encapsulants: EVA (ethylene vinyl acetate), TPO (thermoplastic olefin), and silicone. Commonly used metals in front-contact and back-contact cells will also be explored: Ag, Al, and Cu.

BUDGET PERIOD 1: WORK BREAKDOWN STRUCTURE FOR METALLIZATION CORROSION:

The results of this work were published in three papers: "Using Module Leakage Current Modeling to Understand Corrosion Chemistry", Michael D. Kempe, Peter Hacke, Jichao Li, Katherine Han, Yu-Chen Shen, and Staffan Westerberg [3]; "Electrochemical Mechanisms of Leakage-Current-Enhanced Delamination and Corrosion in Si Photovoltaic Modules" by Jichao Li, Yu-Chen Shen, Peter Hacke, and Michael Kempe [4]; and "Electrochemical Mechanisms of Leakage-Current in Photovoltaic Modules" by Michael Kempe, Peter Hacke, Joshua Morse, Jichao Li, Yu-Chen Shen, and Katherine Han [5].

1-Task 1: Design test structures and induce metallization corrosion on the test structures. *(M 1-M 10) NREL and SunPower*

Task Summary: *NREL and SunPower together will design coupons and test structures to monitor metallization corrosion which will be induced in damp heat chambers and under an applied bias (either with a foil on the glass or a grounded frame nearby). Extensive analysis of the coupons and test structures will be initiated.*

Task Details: *The risk in this task is the identification of suitable test structures that mimic coupon level corrosion. Risk mitigation is to build test structures with the same type of metallization as in the actual cells.*

Subtask 1.1: Design coupons and suitable test structures to mimic corrosion in the cell.*(M I-MS) NREL and SunPower*

A paint corrosion-testing cell was used to conduct electrochemical testing of front-contact cells (FCCs) and back-contact cells (BCCs) in deionized water [6], Figure 1. The FCC cells were typical commercial Al back surface field cells, and the BCC cells were commercial SunPower cells. The total test area was 13.1 cm^2, with a solution volume of 40 mL. Vacuum grease was applied to the O-ring to prevent water leakage between the corrosion cell and the samples. A graphite rod was used as a counter electrode, while a saturated calomel electrode (SCE) was employed as the reference electrode. The cathodic polarization measurement was initiated from 10 mV vs. open circuit potential after 10 min delay in the deionized water (to obtain steady-state), and the scanning rate was 0.5 mV/s. Si cells were rinsed with ethanol and deionized water to clean the surface and were then dried using compressed air.

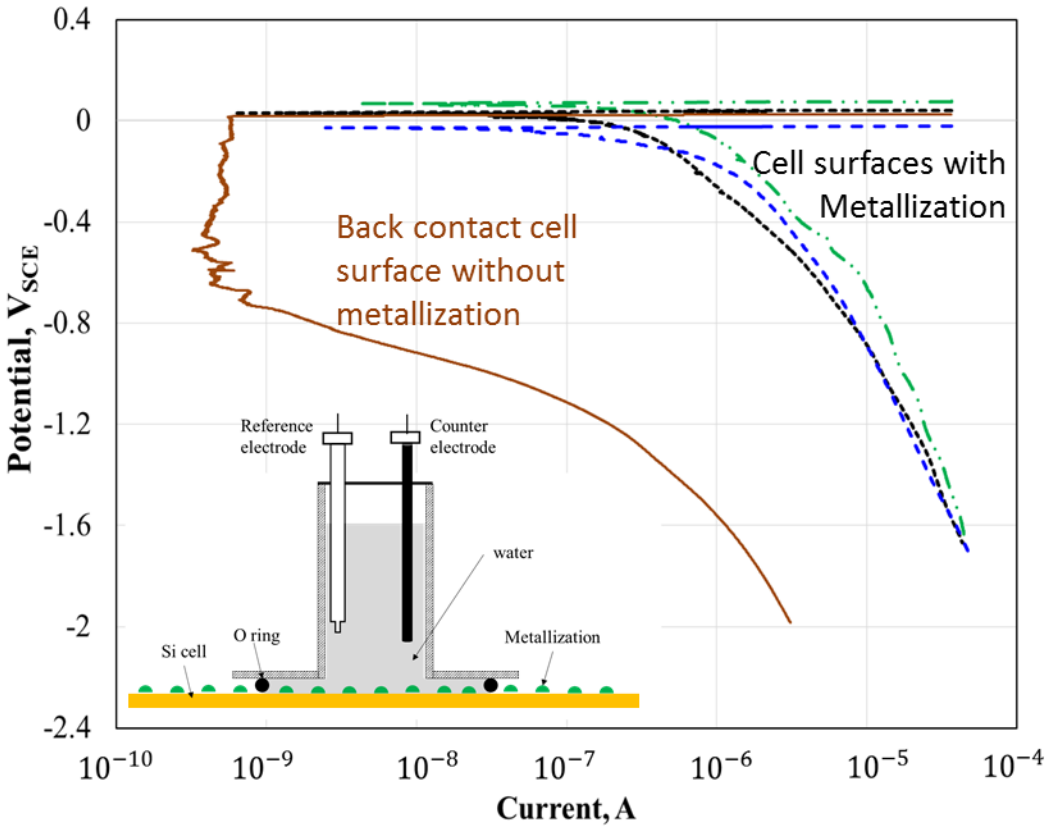

Figure 1. Cathodic polarization curves of front-contact cells and back-contact cells in aerated DI water (the total test area is 13 cm2). Brown line – Front side of back contact cell. Blue line – Back side of back contact cell over metallization. Black line – front side of front contact cell over metallization only. Green line – front side of front contact cell over metallization and tabbing.

The current vs voltage was measured on front contacted cells and interdigitated back contacted cells in an aqueous solution, with respect to a calomel reference cell, Figure 2. Here it was found that front side of front contact cells had about a 10× to 100× higher current for the same voltage. This is explained by the better catalytic and/or electronic properties of the metal surfaces. In the back contacted cells, the surface consists of a SiN_xO_y which must either pass electrons/holes or ions to enable electrochemical reactions and current to pass. In this case charged species accumulate at the surface creating an electric and electrochemical voltage in opposition to the applied voltage.

This accumulation of ions acts as a capacitor providing some storage and discharge of electric charge. In a cell with front metallization, one would expect charged species to accumulate at the SiN_xO_y surface with very slow permeation through it. For a negatively biased cell, accumulated positive ions would drift along the cell surface towards the metallization, down a concentration and voltage gradient, where the electrochemical splitting of water to form OH^- can occur. For a positively biased cell, negative ions would similarly accumulate and move towards the metallization where they could either split water to form O_2 or oxidize the metallization itself.

In negative bias testing, metallization on the cells acts as a cathode, while the grounded frame or the other counter electrode is an anode Figure 2. The high potential between the metallization and the frame, which can be up to -1500 V, induces a leakage current through an electrical field in the encapsulant, glass, and antireflective coating on the cell. In the glass, charge carriers with a positive charge, (e.g. Na^+, K^+, Ca^{2+} or Mg^{2+} ions), migrate to the metallization through the encapsulant. Because of the high abundance in glass and its relatively high mobility, Na^+ is expected to be the dominant positive ionic charge carrier. However, electrons, the only charge carrier in the metal, flow to the cathodic metal. Because there is a difference in charge carriers, electrochemical reduction reactions must occur at the encapsulant/metallization interface to transfer the charge. At the cathode, the only species available to be reduced are oxides or the ionic species. But the SiO_xN_y is very stable, and Si, Na, K, Ca, or Mg metals are unstable in the presence of dissolved water; therefore, the most likely reduction reagent is water. In a humid environment, moisture can diffuse into modules through the backsheet and the encapsulant [7], supplying water for this chemical reaction.

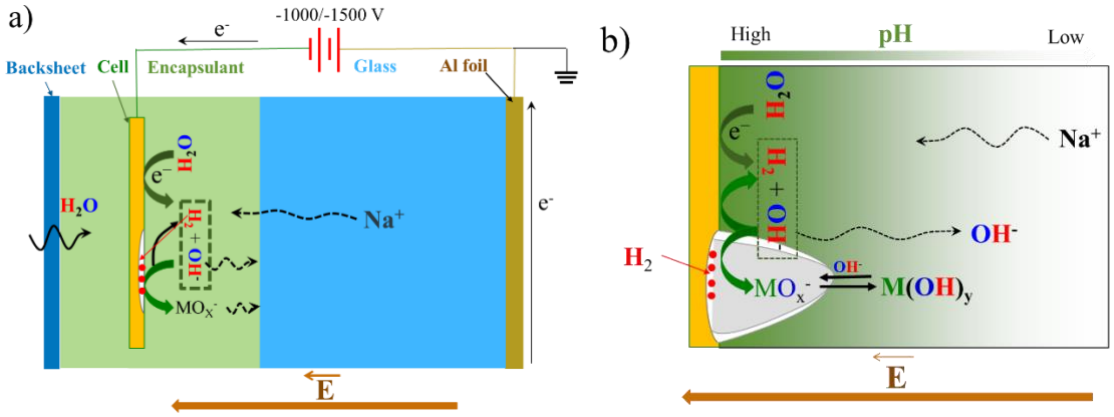

Figure 2. a) Schematic diagram showing ion migration and electrochemical reactions on the metallization under negative bias conditions. b) Close-up schematic of the diagram in Figure 2a, where the green shading represents the basicity. M represents a materials in Si solar cell that is susceptible to corrosion in alkaline solutions.

Subtask 1.2: Induce corrosion in coupons and test structures by placing coupons and test structures in damp heat *(MS-Ml 0) NREL and SunPower*

The first test sample configuration was a 4-cell mini-module Figure 3, first stressed at 85°C/85% RH damp heat (DH) for 1000 hrs according to IEC 61215-2 MQT 13 and then negatively biased (at -1000 V) for 292 hrs with an Al foil placed on the glass in an environmental chamber at 72°C/95% RH [8]. These four-cell mini-modules were constructed for exploring accelerated stress test conditions that reproduce delamination. They were constructed with layers consisting of; glass (tempered, low Fe)/EVA/cells/EVA/polyethylene terephthalate (PET) and Tedlar. The cells were conventional $n^+/p/p^+$ back surface field cells with screen printed metallization including three bus bars of 1.5 mm width, Ag grid finger of approximately 70 µm width in a 1.8 mm pitch. Lead-tin solder coated tabbing ribbon was used. The stress sequence used was non-optimized and exploratory in nature to find accelerated stress conditions to reproduce the delamination mechanism found in the field [8]. Delaminated regions were analyzed in this study by scanning electron microscope (SEM) coupled with energy-dispersive X-ray spectroscopy (EDS).

A second type of sample was made and exposed to negative bias testing (-1000 V) at 85ºC/85% RH in an environmental chamber for up to 300 h. These samples consisted of Sn-coated Cu ribbon, without using a PV cell. A front ~100 µm thick, polyolefin-based encapsulant on the Cu ribbon was used in one test construction and EVA used in a second. A pH paper was placed on the front of the ribbon laminated using glass, with encapsulant on both sides, but no cell, to monitor the local acidity. A similar pH paper went through a high-temperature lamination process to check that it still worked properly.

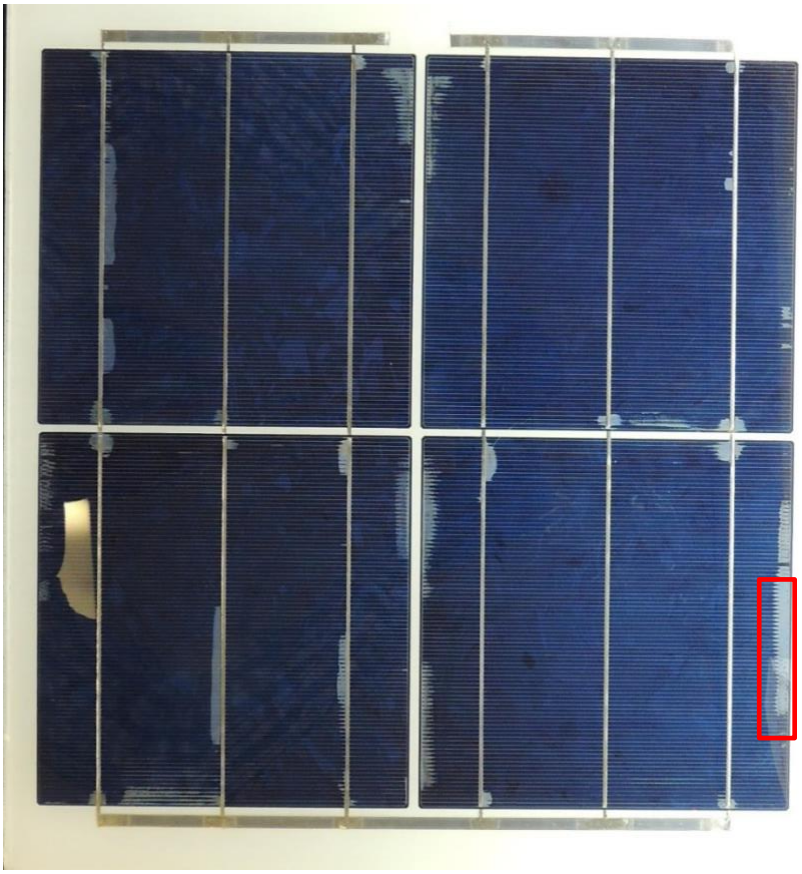

Figure 3. Degraded mini-modules after 292 h bias testing at 72°C/95% RH. Area in red rectangle used for SEM and associated EDS mapping on Ag fingers.

Milestone 1.1.1: *The corrosion progression will be captured. The specific areas of corrosion on the cells will also be identified.*

The Pourbaix diagram in Figure 4 shows the thermodynamic stability of water and Na^+ as a function of potential (relative to a standard hydrogen electrode) at different pH. The equilibrium reduction potential of sodium is far below the reduction potential of water by approximately 3 V [21,23]. This means that water is preferentially reduced when both water and dissolved Na^+ ions are present on the metal surface. Additionally, Na metal is so active that it is stored in a dry inert gas atmosphere or anhydrous mineral oil. If present, reduced Na would be immediately oxidized by oxygen or water vapor. Therefore, the reduction reaction, if any, should be water reduction, generating hydrogen and hydroxide ions, which can be illustrated in the light gray region in Figure 4.

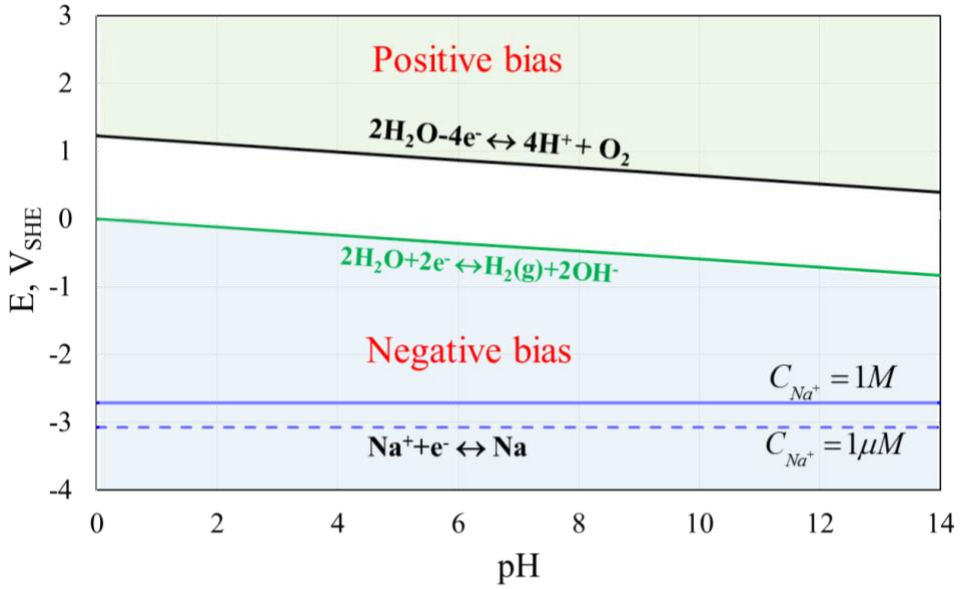

Figure 4. Sodium-water Pourbaix diagram based on the thermodynamic data from Pourbaix [9].

Under positive bias conditions, light green region in Figure 4, water is oxidized generating oxygen and hydronium ions, producing an acidic environment near the metal surface and dissolving metals, through electrochemical reactions, which may also produce acidic oxide species.

The water reduction reactions on the metal surface under negative bias conditions are described by the following equation:

2e- + 2H2O →H2 + 2OH- Equation 1.

The reaction kinetics of water are strongly dependent on the material's catalytic ability given the same experimental conditions. To characterize reaction kinetics on two kinds of cells (front-contact cells and back-contact cells), cathodic polarization curves are measured in DI water using a corrosion cell Figure 1. Current instead of current density is used in this plot, as it is difficult to accurately determine the true metal surface area because of the rough surface. However, with a fixed total test area, the cathodic measurements provide enough information about the relative reaction kinetics on each cell.

The reaction rates are fastest on the front of FCCs with the Ag fingers and Ag busbars centered in the test area and is followed closely by that on FCCs with only Ag fingers in the test area. This kinetic difference is caused by the large metallization coverage due to the presence of the busbar, which also suggests that Ag metallization has better catalytic ability compared to silicon nitride which also retards electron transfer. However, the kinetics on Sn-coated Cu on the backside of the BCCs are like those of the FCCs, although the BCC metal area fraction is much larger than that in FCCs (about 10 x). This difference is attributed to the better catalytic ability of noble Ag than Sn [6], and the large surface area of the rough and porous morphology of the Ag, as shown in Figure 5. The large difference in the catalytic ability by the metallization over the silicon nitride indicates that electrochemical reduction reactions of water caused by the leakage current preferentially occur on the metallization and the associated degradation is expected in the same position. This has been observed in the lab and field and will be discussed later in the report.

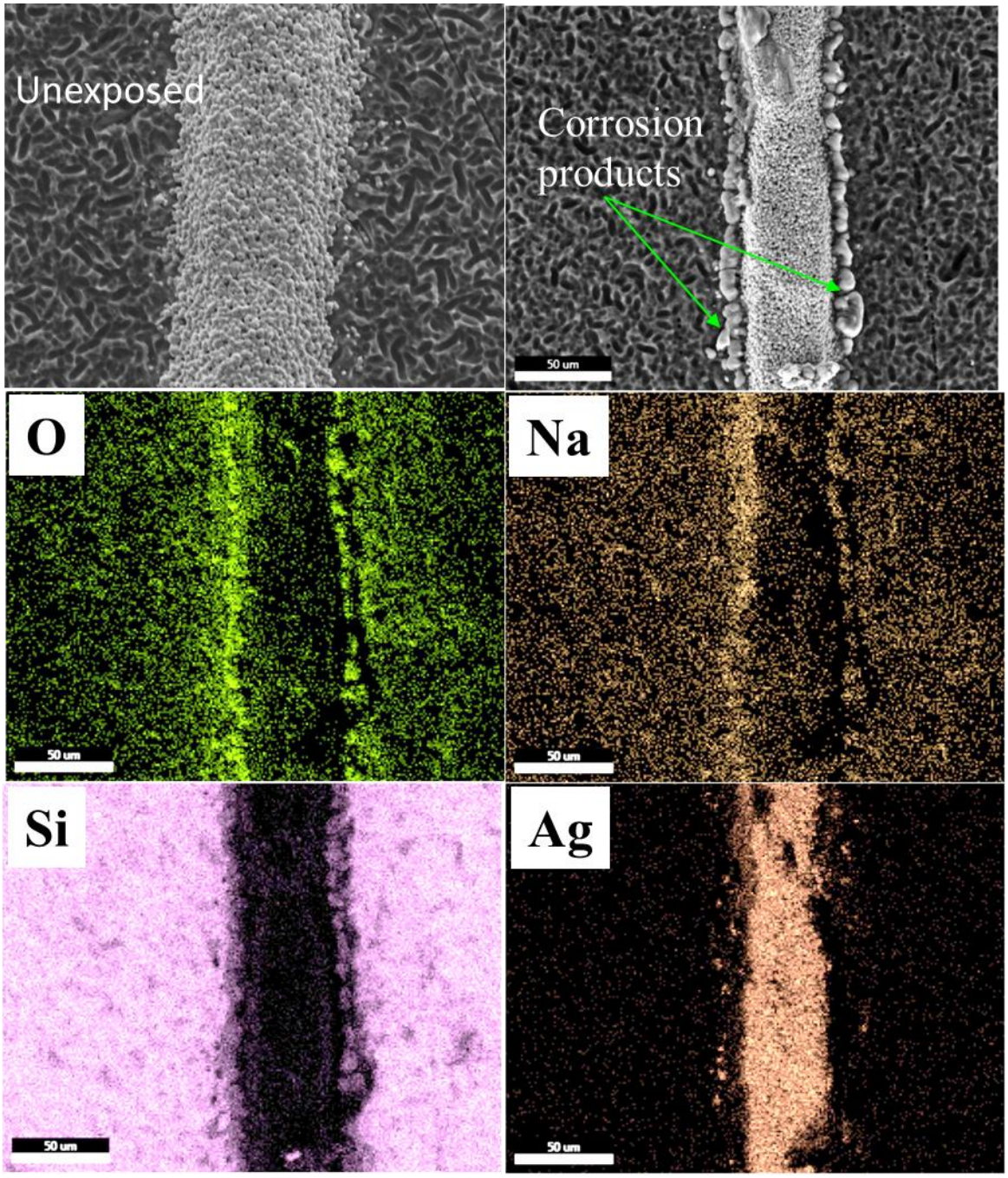

Figure 5. SEM and associated EDS mapping on Ag fingers at the delamination area before and after 292 hrs bias testing at 72°C/95% RH.

When hydrogen gas is evolved as shown in Figure 6, it can escape by diffusion through the encapsulant and backsheet. Only to a small and insignificant extent can H_2 produced on the front side of a cell diffuse through the wafer and out the backside, therefore H_2 produced on the front side must diffuse distances on the order of many centimeters to escape the module. Because the H_2 pressure on the front side can build up significantly, this can promote delamination and/or bubble formation. Figure 6 shows gas bubbles on metallization fingers after bias testing (-1000V) at 85°C/85% RH. These isolated bubbles are spherical and form along the side of the metal finger, which is consistent with electrochemical activities on the metallization and reduced adhesion to Ag [10-12]. These gas bubbles can grow and merge together, leading to large delamination.

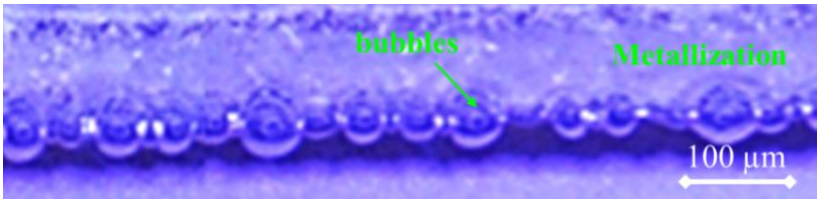

Figure 6. Isolated bubbles on the metallization in the early stage during the negative bias testing (-1000V) at 85 °C/ 85 % RH. The sample was checked weekly, and the bubbles appeared after 4 weeks.

This H_2 gas pressure enhanced delamination is demonstrated in a 27 y ARCO module. Here delamination is not seen near the periphery of the cell where there is sufficient time for H_2 to diffuse out of the modules, Figure 7. But towards the center gas pressure is higher promoting faster delamination. However, it should be noted that this module was constructed with PVB as an encapsulant and would thus have a much higher leakage current and a much greater H_2 production rate.

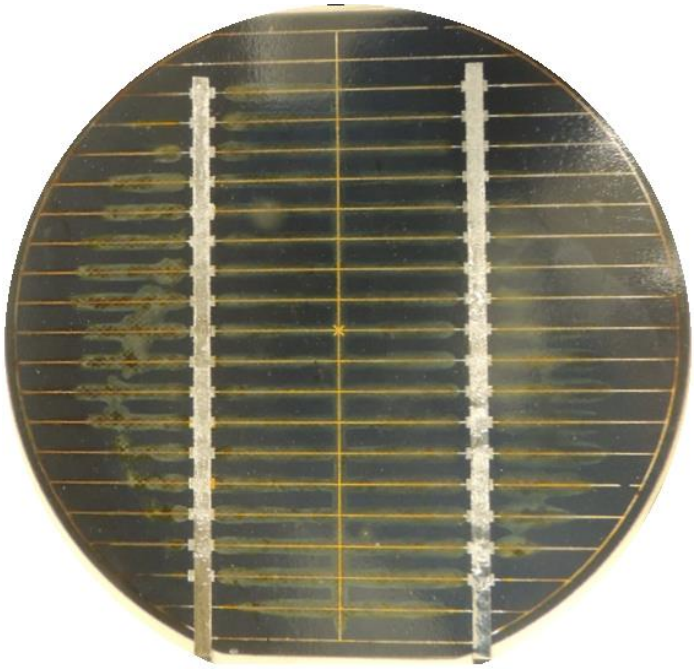

Figure 7. Delamination observed on the metallization in an Arco Solar module after 27 years exposure in the field. Note the delamination blisters along the metallization lines. The metallization appears to be corroded (brown coloring) under the blisters.

1-Task 1 (Subtasks 1.1 and 1.2) Results:

While hydroxide ions are generated through water reduction, mainly near the metallization, they migrate and diffuse into the encapsulant from the surface driven by the electrical force and concentration gradient as shown in Figure 3. An OH^- concentration profile with the highest concentration near the surface is expected. To verify the formation of hydroxide ions near the metallization, a pH paper was laminated between a Sn-coated Cu ribbon and a piece of glass using either EVA or a polyolefin encapsulant. The ribbon was biased at ±1000V relative to the glass it was laminated to, placed in a chamber at 85°C and 85% RH, and the color was checked periodically.

The pH paper in the polyolefin encapsulant turned from the original yellow color to a more orange color after 24 hours of testing indicating the presence of a basic environment, Figure 8. A control sample without bias was also tested under the same conditions, and no color change was observed. A polyolefin absorbs less moisture than EVA and does not produce acetate byproduct. Assuming the limiting step in splitting water is attributable to materials resistivity and/or catalytic activity on metal surfaces and not the presence of water, then the lower amounts of dissolved water would solubility would affect the production rate of acidic or basic chemical compounds. Lower moisture would then result in less hydroxide is needed to change the acidity compared to EVA. In EVA the presence of acetate byproducts, present even in unexposed EVA film directly from the manufacturing process, would be expected to buffer the acidity also making it more difficult to change.

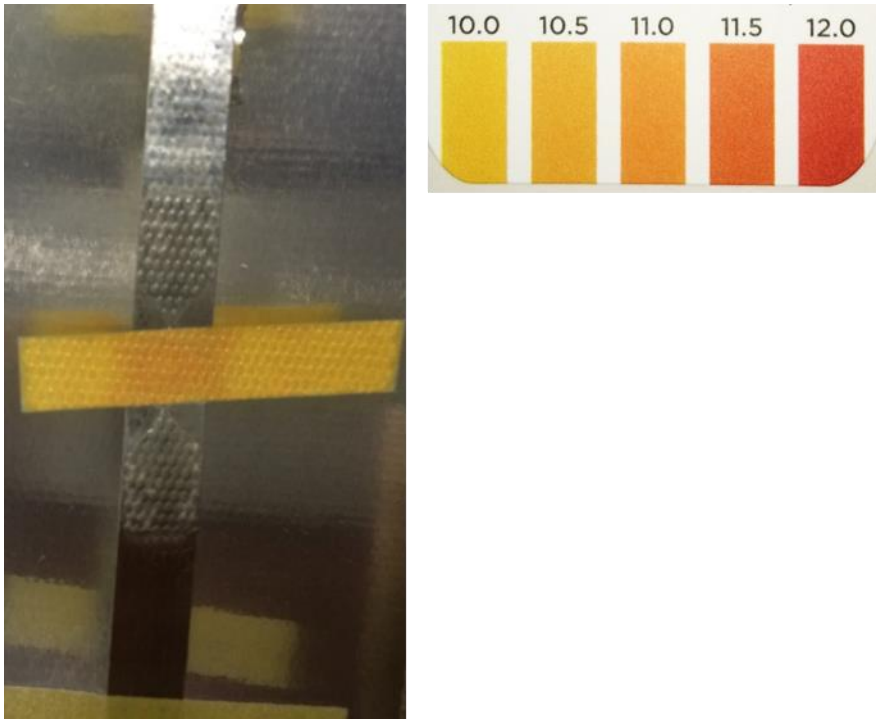

Figure 8 pH paper laminated in to glass using a non-EVA encapsulant on the front of a Sn-coated Cu ribbon during negative bias testing at -1000 V and 85°C/85% RH (the figure on the right is the pH scale). Prior to stress, the pH strip had a uniform color.

As expected, when repeated in the EVA samples it took longer to see the changes, Figure 9. In addition to a negative bias, a positive bias was used to demonstrate that the encapsulant can be driven to either acidic or basic conditions depending on the voltage bias. This indicates that the generation of hydroxide ions can be more important than the acetic acid by-products in EVA in determining the bacisicity of the packaging. Any study looking at degradation processes that may be influenced by bacisity or acidity must account for the voltage bias of a PV device to be accurate.

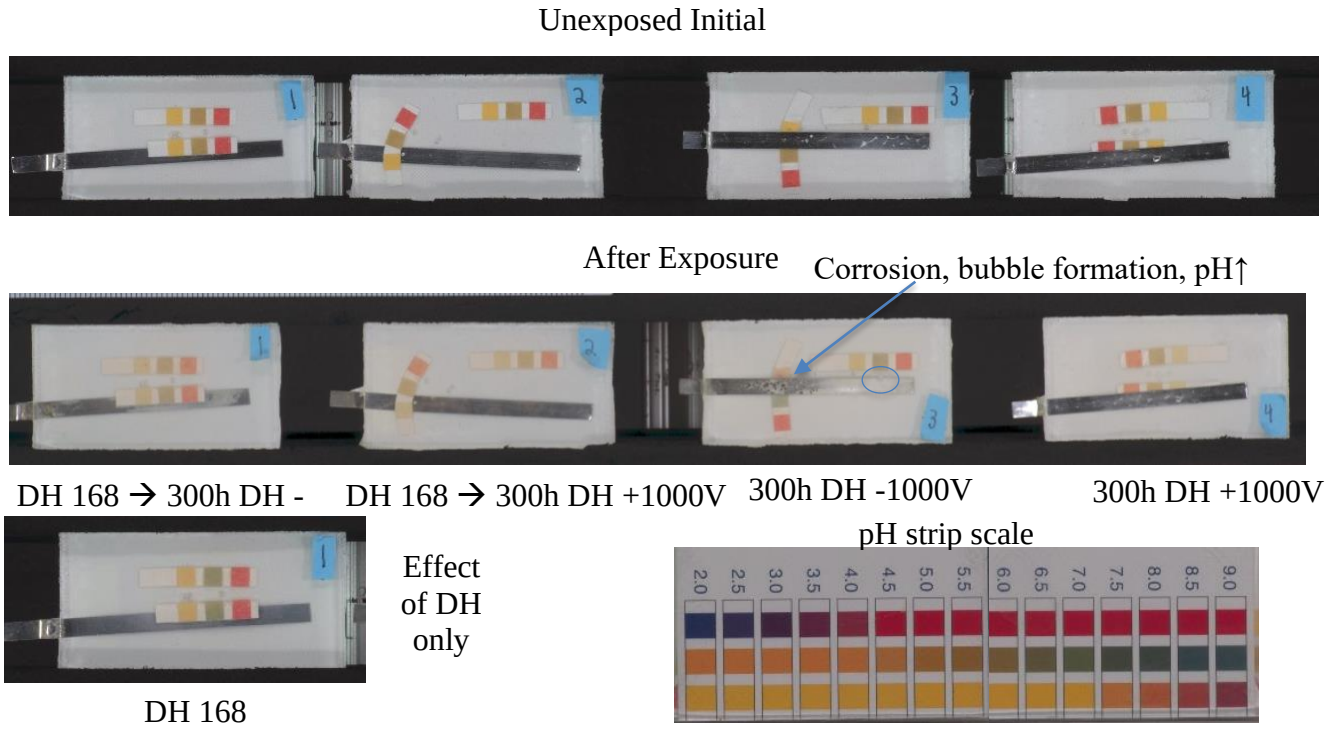

Figure 9 Change in acidity as a function of voltage bias in EVA. Some samples were exposed to 168 h of damp heat before bias was turned on for an additional 300 h with bias. Other samples were put directly into damp heat with bias.

This high basicity near metallization leads to the corrosion of the metallization and the degradation of the SiO_xN_y antireflective coating and the Si semiconductor. The extent of the corrosion is dependent on the corrosion resistance in the basic environment. For example, while Ag is stable at high basicity pH [23], Si or SiO_2 can dissolve or directly electrochemically decompose to form SiO_3^{2-} as described in the following equations [23]:

Si + OH- + H2O → H2 + SiO32-, Equation 2

Si + 2 e- + 3 H2O → 3H2 + SiO32-, Equation 3

or

SiO2 + 2 OH- → H2O + SiO32- Equation 4

Figure 5 shows the morphology of Ag fingers from the delaminated areas in the FCC modules (the rectangular region in Figure 1), and the associated EDS elemental mapping. In the SEM images, granular particles are only observed along the edge of the Ag fingers, which are not observed in the original cells. These particles are enriched in Na, O and Si, but are depleted of Ag. EDS analysis shows that their composition are 44.1 wt.% O, 7.3 wt.% Na, and 40.9 wt.% Si. These data indicates that these particles should be Si corrosion products, not Ag particles from the metallization fingers. 7.3 wt.% Na corresponds to 2.9 wt.% O associated with NaOH (or less in Na_2O), and the rest 36.8 wt.% O should combine with Si. As discussed above, the generated hydroxide ions, which are highly concentrated near the metal fingers, react with the adjacent Si, leading to the formation of silicate. Although there is a protective silicon nitride layer on the surface, the hydroxide ions may still have a chance to react with the Si through openings in the nitride layer such as pinholes or near the metallization where Ag spans the SiO_xN_y film[24][25]. It is also reported that in an aqueous solution, silicon nitride may break down and decompose through reactions with water at high temperature [26], high humidity [26], and high potential [27]. The solid reaction product, hydrous silica [26], can dissolve at high basicity and expose the Si substrate. The hydroxide ions have sufficient contact with the exposed Si, leading to the dissolution of Si. The silicate ions may combine with Na^+ from the glass to form stable sodium silicate, as schematically shown in Figure 10. Similar Na-rich precipitates have previously been observed on the silicon nitride and near Ag metal finger after exposure to damp heat and bias [4]. However, Ag fingers are immune to corrosion in alkaline environments with negative bias [28], and no corrosion products are on the Ag fingers as shown in Figure 5.

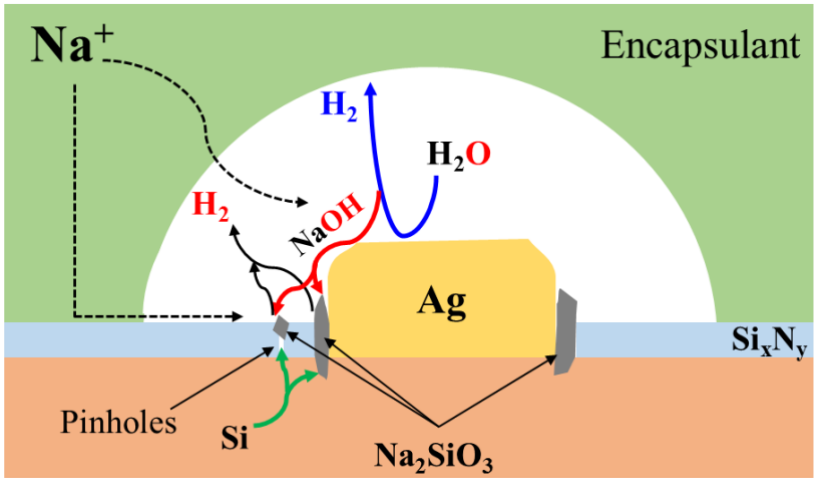

Figure 10 Schematic diagram showing Si corrosion near Ag fingers and at defects or pinholes in the SiOxNy during negative bias testing.

The corrosion and delamination caused by the electrochemical reaction on cell metallization are dependent on the leakage current. Even though the voltages applied to a module are on the order of ±1500 V, the voltage applicable to the electrochemical reactions, Figure 4, are much less. As the charge flows through the glass and the polymer, the voltage potential drops until there are just a few volts as are needed to promote electrochemical reactions at the surfaces where current changes from ionic to electronic. For the formalism of the Pourbaix diagram (Figure 4), the resistance of the solution is negligible such that the kinetics are governed by the energetics of the reaction chemistry, but in the PV module it is the resistance to charge transfer that limits the energetics with the final voltage of the chemical reaction being a negligible contribution.

Several factors affect leakage current, including bias potential, and resistance of both glass and encapsulant, which are a function of temperature[17], humidity[17], and impurities [19]. Under negative cell bias, the ionic component of the leakage current can cause electrochemical reduction reactions, producing hydrogen and hydroxide ions, as the charge carriers change at the cell/encapsulant interface. Besides the water reduction reactions, Si corrosion reaction with the generated hydroxide ions also generates a small amount of hydrogen as shown in Equations 2 to 4. Hydrogen gas accumulates on the metal surface and promotes delamination. The hydroxide ions change the local environments near the metallization, and corrosion of materials such as Si or SiO_2 under the alkaline environment damages the bonding between encapsulant and solar cell. Furthermore, the corrosion products are voluminous and promote delamination. Corrosion and delamination are interactive and promote the formation and propagation of one another.

1-Task 2: Model and measure leakage currents in the coupons *(M6-Ml 5) SunPower*

Task Summary: *A model will be built from a program package like Comsol. Resistivities of the encapsulant at various T and RH will be measured as inputs to the model. Leakage currents in different parts of the coupons will be measured to compare to the model.*

Task Details: *A risk is the accurate measurement of I_{leak} in the cell. To mitigate the risk, many probes will be placed in different areas of the cell. Another risk in this task is a model that is inaccurate, which can be mitigated by first verifying simple models before building full models.*

Subtask 2.1: Measure the resistivities of materials in the coupons and I_{leak} in the coupons. *(M10-M13) SunPower*

Subtask 2.2: Construct an electrical model of coupons/modules and compare to experimental data. *(M10-M15) SunPower*

Milestone 2.2.1: *An electrical model of the coupon or module is built and compared to experimental data. If enough data is collected, the information will be prepared for journal articles and conference talks.*

1-Task 2 (Subtasks 2.1 and 2.2) Results:

Subtask 2.1 material resistivity results:

Similar to what is reported elsewhere [13], volume and surface resistivity measurements were performed in a Keithley 6517A electrometer with an 8008 resistivity fixture surrounded by a copper mesh Faraday cage to reduce sources of signal noise. For these measurements, an On/Off cycle was used switching between 0 V and 1000 V every 12 hours according to IEC 62788-1-2 [4]. The 8008 fixture was placed in an ESPEC BTX-475 environmental chamber enabling measurement as a function of temperature and relative humidity. For polymer measurements, thin films, ~0.46 mm thick, were given at least 24 h to equilibrate to the chamber atmosphere prior to measurement.

Resistivity measurements were performed on commercially available poly(ethylene-co-vinyl acetate) (EVA), a thermosetting polyolefin elastomer (POE), and a low iron soda-lime glass with texturing on one side (see Table 1). The EVA and POE were cured using a vacuum lamination cycle, lasting 15 min, with a bed temperature of 145°C. We were not given, and did not obtain, specific information detailing the composition of these encapsulants, therefore specifically divulging the identity of the materials would not add to the scientific understanding of these materials. The data here is intended to demonstrate typical properties of these classes of materials relevant to leakage current. We had wanted to study polymer effects more thoroughly, but just understanding EVA and POE proved to be more difficult than anticipated. Regardless, EVA and POE are much more relevant to typical PV constructions.

For the glass sample, measuring the surface conductivity requires the flat side to span the annular electrode gap over which the measurement is made, Figure 11. For the glass volume resistivity however, the textured side could not be used to contact an electrode, therefore two pieces were laminated together with the smooth side facing outward using an electrically conductive adhesive. The samples were only 50.8 mm × 50.8 mm to fit entirely between the electrodes and cover most of the smaller inner electrode area. This creates a small amount of systematic measurement error because of a small amount of uncontacted area on one side and lateral conduction in the conductive adhesive, but this approximately 5% inaccuracy is unimportant.

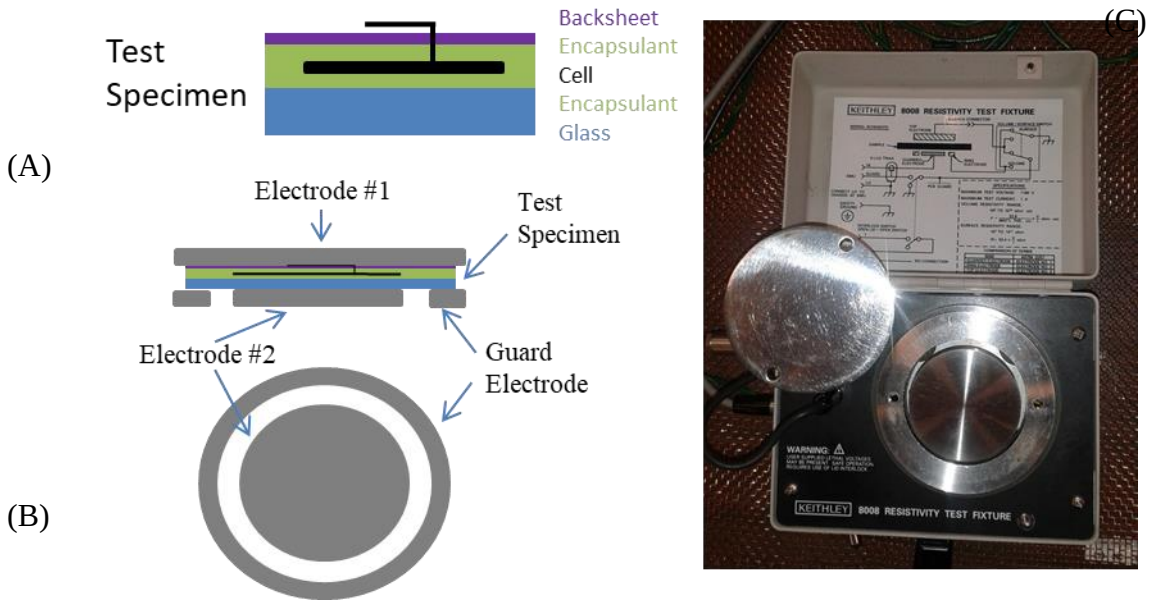

Figure 11. (A) Schematic of test specimen. (B) Schematic of electrode. (C) Photograph of electrode fixture.

Measurements of surface and volume resistivity of these materials were conducted at 25˚C, 45˚C and 85˚C and at relative humidities of 5%, 50%, and 95% at all these temperatures. For the glass volume resistivity, the RH was kept low at 5% to minimize measurement error attributable to lateral current flow.

The volume resistivity, *R*, was measured on glass and on two encapsulant materials and were fit to an Arrhenius model [14] as,

$$R = R_0 e^{-\frac{E_a}{RT}} e^{RH \cdot a}, \quad Equation\ 5$$

where R_o is a prefactor constant, *Ea* is the activation energy, *R* is the Universal Gas Constant, *RH* is relative humidity and *a* is a constant related to relative humidity. The surface resistivity for glass was also fit to Equation with *a*=0. These fits were accomplished using the statistical software JMP such that the uncertainty in the various parameters could also be calculated, Table 1. For these fits, the correlation between *ln(Ro)* and *Ea* was always near unity but the correlation between a and *ln(Ro)* or *Ea* was negligibly small. The individual data points for select materials are shown in Figure 13 along with some of the fit lines from Equation 5 and Table 1. This indicates the reasonableness of the model when one considers that getting reproducible measurements within a factor of two for the resistance of insulating materials is good [15]. The only exception to this is for the surface resistivity of glass for which there is a large uncertainty relative to the value. We believe that this is possibly explained by the sensitivity of this surface to contamination [16]. It is possibly because this is a very different measurement than bulk resistivity and that good contact of the electrodes to the slightly bumpy surface (on the flat side) of the rolled glass may be inadequate.

Table 1. Resistivity Parameters for all materials tested. Determined as a JMP nonlinear fit to Equation with the associated uncertainties and correlation coefficients. The correlation coefficients with Ro subscripts refer to the correlation with ln(Ro).

	ln(Ro)	Ea	a	CorrRoEa	CorraEa	CorraRo
	ln (Ω·cm) or ln(Ω/□)	(kJ/mol)	(1/% RH)			
EVA Resistivity	-5.03±4.89	-102±6	-0.013±0.005	0.999	0.117	-0.010
Glass Volume Resistivity	-2.34±0.42	-84±1	NA	0.997	NA	NA
Glass Surface Resistivity	-2.7±5.4	-99±14	-0.098±0.012	0.991	0.050	-0.066
POE-1 Resistivity	6.56±2.28	-84±6	-0.014±0.005	0.999	0.103	-0.025
POE-2 Resistivity	9.68±1.92	-74±13	-0.015±0.011	0.999	0.117	-0.010
Silicone Resistivity	23.69±1.92	-29±5	-0.011±0.004	1.000	0.134	0.012

This large, exponential dependence of resistivity on RH is expected in polymeric materials [17] and can be explained by either the water bonding to ionic species to help separate them from ionic moieties on the polymer, by electrochemical splitting of water to create ionic species for charge transfer, or plasticization of the polymer backbone [18]. Similarly, the values for the thermal dependence of resistivity are a little higher in EVA compared that of the polyethylene based material, but low relative other more polar polymers generally as reported in the literature [14], Figure 12.

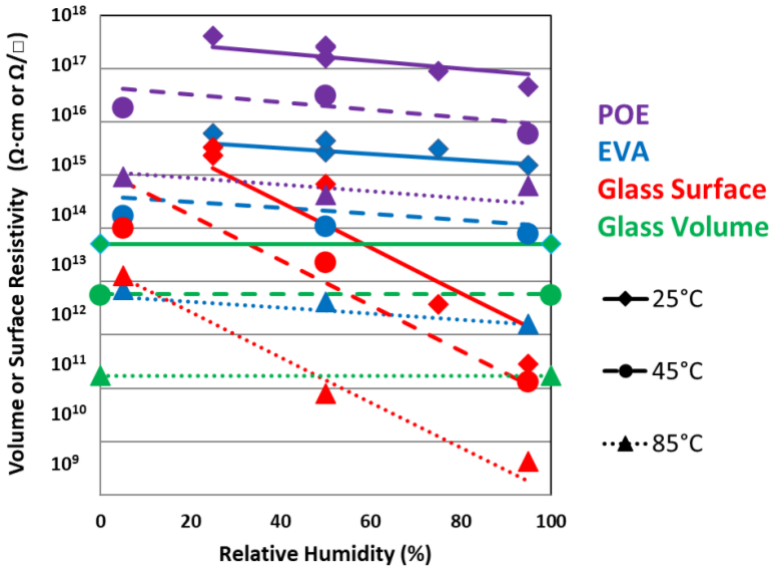

Figure 12. Plot of measured and modeled resistivity data for materials examined in this study.

A polymer may, depending on the climate, experience humidity from around 10% RH during the day to upwards of 90% RH at night. Seasonal effects further result in about a 30% change in absolute humidity [19]. But because of the high activation energy for resistivity, Table 1, it is the thermal effects that dominate the conductivity of the polymers especially through the diurnal cycles. Therefore, in modeling the leakage current the contributions from the bulk conductivity of polymeric components is primarily governed by thermal effects. For the glass surface conductivity however, it is the surface RH that dominates [16, 20].

For a morning temperature increase from 20˚C and 100% RH and ending at 40˚C and 31.2% RH (assuming the absolute humidity is constant), Table 1 would predict a decrease in the surface conductivity of 63×. This explains most of the reasons that humid environments experiencing a lot of dew are more prone to potential induced degradation and that most of the leakage current is seen in the morning [16, 20-22]. Higher leakage current is not attributable to moisture absorbed in the polymeric materials. Dew on a module in the morning takes some time to evaporate off allowing the module to heat up while maintaining a very high surface RH causing a large increase in conductivity. If only half of the surface is covered with dew, one would see something on the order of a doubling of the conductivity as the water covered areas could be considered highly conductive relative to the dry areas. So even the separation of water droplets would not be expected to dramatically decrease the surface conductivity until the surface is nearly free of condensed water.

This demonstrates how the surface conductivity [23] represents a large source of variability in the leakage current that is highly susceptible to the effects of water and similarly to dust and other pollutants in the air.

Subtask 2.1 coupon measurements:

The same Keithley 8008 resistivity test fixture and Keithley 6517A electrometer were used for transient current measurements but with a computer recording the data using a LabVIEW program utilizing an IEEE-488 interface. The test coupon was designed to duplicate the current flow characteristics perpendicular to the cell through the glass while ignoring the effects of lateral current conduction across the glass, Figure 13. Cells were cut to 50.8 mm × 50.8 mm squares using a U.S. Laser Corp. Model # 4024/5024 Nd:YVO4 laser scriber operated at double-frequency of 532 nm with a pulse-width of ~ 5 ns. The glass is cut to 63.5 mm × 63.5 mm squares. The backsheet is a common polyethylene terephthalate containing material. Essentially no current will pass through the backsheet, therefore its exact composition is unimportant. The cell is sized such that the corners of the cell extend to the outer diameter of Electrode #2, Figure 11. The back contact (BC) cells were provided by SunPower and the front contact (FC) cells were typical industry multicrystalline aluminum back surface mono facial cells. Voltage is applied via some tabbing extending through the backsheet with direct contact with Electrode #1, Figure 11. While some current can pass from Electrode #1 to Electrode #2 directly past the cell in the perimeter area, this area is much smaller, and the current density is much less than that passing through the cell making it insignificant. With this setup, the effective area is essentially equal to the area of the cell. This effectively provides 1-D current flow between the cell through the encapsulant and glass to the electrode.

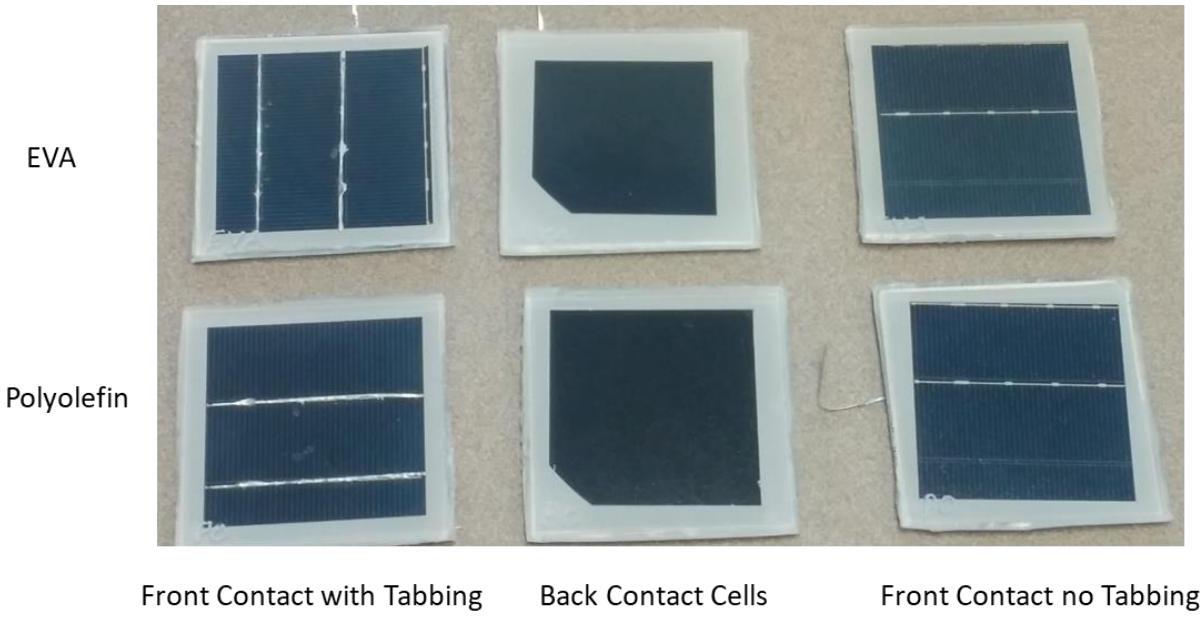

Figure 13. Photograph of test samples used in this study. Cells were cut to 50.8 mm × 50.8 mm squares. This contains photos of all the samples used in the study, but several measurements were made on some of the samples under different conditions and at different times.

Two Dimensional Transient Current Measurement in PV Cells

In another experiment, a set of single cell mini-modules was created with the same materials but with a conductor placed on the perimeter to simulate a frame Figure 14B. The frame was grounded and ±1000 volts was applied to the cell and the transient leakage current was measured, Figure 14A.

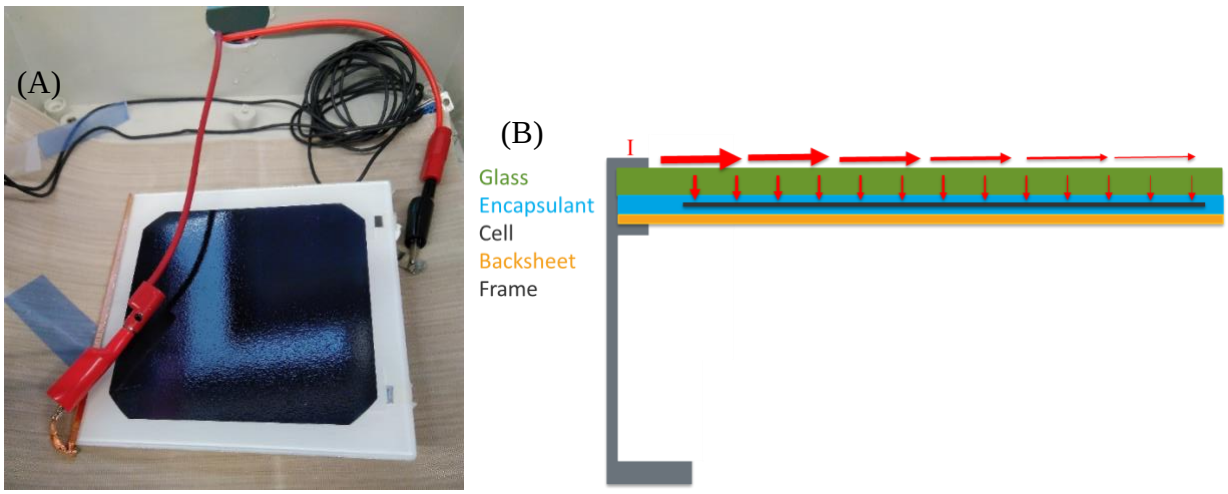

Figure 14. (A) Image of a cell with a copper foil used on the edge of the single cell mini-module to simulate a frame. Here the copper foil is at ground and the voltage is applied to the cells using the tabs coming out from the backsheet. (B) Schematic of the current flow in a PV module.

Subtask 2.2 and Milestone 2.2.1 results

At night the voltage between PV cells and a grounded frame essentially goes to zero but there is an amount of leakage current resulting from the dissipation of charge in the module. This charge may be a residual effect of capacitance and/or electrochemical reactions. In the experimental set up for samples in Figure 11, the PV cell and electrode #2 act as the top and bottom of a set of capacitors with some current leakage in the form of the movement of electrons and or ions from material to material. At interfaces there will be changes in the mobility and concentration of electrons and ions leading to charge build-up. There are also electrochemical reactions at the interfaces anytime the conduction switches between electronic and ionic. This can be the conversion of a water molecule and an electron to hydrogen gas and a hydroxyl group, or hydroxyl groups to oxygen gas, water and electrons, Table 2. Alternatively, just the nature of the mobile ionic species may change reducing the flow of charge creating charge build-up and consequent electric fields.

Table 2: Candidate electrochemical and ion exchange reactions possible at various interfaces. Red font is for electrochemical reactions and Black font is for ion exchange reactions. Yellow highlighted items are believed to be the more prevalent reactions. These reactions should be viewed as representative as there are many different reactions possible and mixed ionic salts or hydrated salts are possible.

Cell At Negative bias	**Cell At Positive bias**
Aluminum to Glass	Aluminum to Glass
$3\ OH^- + Al \rightarrow Al(OH)_3 + 3\ e^-$	$\equiv Si\text{-}OH + AlO(OH) + e^- \rightarrow Al(OH)_3 + \equiv Si\text{-}O^-$
$2 \equiv Si\text{-}O^- + H_2O \rightarrow 2 \equiv Si\text{-}OH + ½\ O_2 + 2\ e^-$	$Na^+ + Al(OH)_3 + e^- \rightarrow NaOH + AlO(OH) + ½\ H_2$
$\equiv Si\text{-}O^- + Al(OH)_3 \rightarrow \equiv Si\text{-}OH + AlO(OH) + OH^-$	$Ca^{2+} + 2\ Al(OH)_3 + e^- \rightarrow Ca(OH)_2 + 2\ AlO(OH) + H_2$
	$7\ H_3O^+ + Al_3O_2 + e^- \rightarrow 3\ Al(OH)_3 + 7\ H_2$
Glass to Polymer:	Glass to Polymer:
$\equiv Si\text{-}O\text{-}Na \rightarrow \equiv Si\text{-}O^- + Na^+$	$\equiv Si\text{-}O^- + Na^+ \rightarrow \equiv Si\text{-}O\text{-}Na$
$\equiv Si\text{-}OH + OH^- \rightarrow H_2O + \equiv Si\text{-}O^-$	$H_3O^+ + \equiv Si\text{-}O^- \rightarrow \equiv Si\text{-}OH + H_2O$
$\equiv Si\text{-}O\text{-}Na \rightarrow \equiv Si\text{-}O^- + Na^+$	$\equiv Si\text{-}O^- + H_2O \rightarrow \equiv Si\text{-}OH + OH^-$
$\equiv Si\text{-}O\text{-}CaOH \rightarrow \equiv Si\text{-}O^- + CaOH^+$	$\equiv Si\text{-}O^- + Na^+ \rightarrow \equiv Si\text{-}O\text{-}Na$
$2 \equiv Si\text{-}O^- \rightarrow \equiv Si\text{-}O\text{-}Si\equiv + ½\ O_2 + 2\ e^-$	$\equiv Si\text{-}O^- + CaOH^+ \rightarrow \equiv Si\text{-}O\text{-}CaOH$
	$\equiv Si\text{-}O\text{-}Si\equiv + H_2O + e^- \rightarrow 2 \equiv Si\text{-}O^- + H_2$
	$H_2O + \equiv Si\text{-}O^- \rightarrow \equiv Si\text{-}OH + OH^-$
Polymer to SiN_xO_Y	Polymer to SiN_xO_Y
$SiN_xO_Y + 2\ OH^- + (1\text{-}y)\ H_2O \rightarrow (SiO_3)^{2-} + x\ NH_3 + H_2$	$SiN_xO_Y + 2\ OH^- \rightarrow (SiO_3)^{2-} + x\ NH_3 + (1\text{-}y)\ H_2O$
$H_20 + e^- \rightarrow OH^- + ½\ H_2$	$3\ H_2O \rightarrow 2\ H_3O^+ + ½\ O_2 + 2\ e^-$
$SiN_xO_Y + 2\ Na^+ + (3\text{-}y)\ H_20 + \rightarrow Na_2SiO_3 + x\ NH_3 + 2\ H_3O^+$	
$SiN_xO_Y + H_2O + e^- \rightarrow (SiO_3)^{2-} + x\ NH_3 + (2/3\text{-}x)H_2 + (y\text{-}1)\ H_2O$	
Polymer to Gridlines/Metallization	Polymer to Gridlines/Metallization
$2\ H_2O + 2\ e^- \rightarrow OH^- + ½\ H_2$	$3\ H_2O \rightarrow 2\ H_3O^+ + O_2 + 2\ e^-$
$M^{n+} + e^- \rightarrow M^{(n-1)+}$ (M=Ag, Sn, Pb, Cu…)	$M \rightarrow M^{n+} + n\ e^-$ (M=Ag, Sn, Pb, Cu…)
PV Cell to AR coating	PV Cell to AR coating
$Na_2SiO_3 + e^- \rightarrow Na + NaSiO_3^-$	$Si + OH^- \rightarrow \equiv SiH + ½\ O_2 + e\text{-}$

An example of interfacial charge build-up was demonstrated at the cell anti-reflective (AR) coating to polymer interface [3, 4, 24]. While some Na^+ ions have been shown to be able to cross through the AR coating to create shunts in the PV junction [25], this process is partially reversible reversible through out-diffusion [26]. The reversibility indicates that it occurs without large scale damage and it is further known that the composition of the AR coating, and its consequent ionic conductivity, is highly influential on a cells resistance to potential induced degradation and preventing the migration of Na^+ ions to the cell [27]. For a good AR coating, charged species will accumulate at the polymer to AR coating interface, generating an electric field through the AR coating. There is also a component of the electric field at this surface in the direction of the gridlines.

The resistance of electrons and other charge carriers to crossing the AR coating was noteably observed by SunPower where it was implicated in a reduction in carrier lifetime reductions as a result of surface polarization [24, 28]. When the cells were under positive bias there is a build-up of negative charge on the outside of the AR coating, at the polymer to SiN_xO_y interface. This causes positively charged light-generated holes to accumulate at the front of the cell/AR coating interface where they combine with electrons in the n-type silicon increasing the surface recombination velocity. When stressed in a chamber under bias in the dark, there is an efficiency loss which is regained upon exposure to light. This indicates that the AR coating becomes photoconductive. Thus there is evidence of electron movement through the AR coating but with some migration of Na^+ ions through at least some AR coatings. These observations support the idea that there may not be significant electrochemical reactions at the cell to AR coating interface but some minimial electron conductivity in the AR coating allowing electrochemical reactions to occur primarily at the polymer to AR coating interface, Table 2.

At the gridlines, there is both the availability of water molecules and oxidizable metals or conversely, reducible metal oxides. Previously, we showed that under negative cell bias, this results in the corrosion of the AR coating to silicates near the gridlines interface [3, 4]. This is presumably either through direct electrochemical corrosion or through the formation of basic species which enable the corrosion of the AR coating under negative bias. At positive bias, the environment would tend to be acidic, which does not disolve silicates like a strong basic environment. With positive bias, one would expect to see some dissolution of the gridlines themselves which has been observed historically when relatively highly conductive polyvinyl butyral (PVB) have been used, and to a lesser extent with EVA encapsulants [4, 29-32].

In the polymer, most of the current conduction is through ionic species, but there would be expected to be some amount of electron based current flow. The difference in the relative contributions could be as high as many orders of magnitude. These ions will be generated or consumed at the glass or at the metallization primarily. But with a material such as glass, if ions are continually removed a more pure SiO_2 layer will be formed at the interface. This can in turn produce a region resistant to ion flow and hold charged species on both sides leading to an increase in charging and a reduction in overall conductivity. Being a thin and potentially highly insulating layer, the capacitance can be relatively large. These kinds of effects can also change the nature of the conduction to favor the movement of electrons over ions.

Na^+ is not the only species that can flow through the polymer but it is the primary one implicated in PID degradation of Si cells through its specific ability to incorporate itself into the crystalline lattice [25, 33-36]. Other possible conductive species include OH^-, H_3O^+, K^+, Ca^{2+}, $Fe^{2+,3+}$, Ag^+, Mg^{2+}, & etc. Presumably, these other species are not easily incorporated into the Si lattice and/or their effects are less important. The relative contributions of these different species is unknown, but smaller and monovalent ions would be more mobile, and of course higher prevalence would be a significant consideration too. The direction of flow is dependent on the bias and on the charge of the species. For OH^- and H_3O^+ this is important because they can be produced at different interfaces and move in the opposite directions to produce the same net current. Species like Fe and Ag can be plated out on surfaces, but Ca and Mg are reactive such that they would be expected to oxidize upon reaction with water to form hydrogen gas and hydroxides which could further diffuse down concentration gradients.

In soda-lime glasses the dominant form of conduction is through smaller monovalent cations, most noteably Na^+. Because of this, it is expected that the electrochemical reaction enabling the change from electron to ion conduction occurs almost exclusively at the Al-frame to glass interface. Depending on the bias this is primarily the result of either Na^+ motion and/or $\equiv Si\text{-}O^-$ production in the glass to redoxively produce H_2 or O_2 at the Al frame interface or to oxidize Al when the cell is at negative bias. At the glass to polymer interface, primarily ion exchange reactions are occuring. This can result in the removal/addition of Na^+ or other cations from/to the glass, or the production/consumption of OH^- in the polymer. If Na^+ is removed from the glass it will be depleted from the surface resulting in the formation of a more highly resistive layer [37] which may in turn result in charge build-up at its interfaces.

Electric Field Driving Forces for Transient Voltage Relaxation Modeling

In the test samples, Figure 11 and Figure 13, current conduction is essentially one dimensional. In a PV module, the current must travel laterally across the glass before going through the glass and polymer to the cell. The resistivity in the polymer is so much greater than the glass, Figure 12, that there is no significant lateral conduction in the polymer. Comparison of the glass surface to the bulk conduction is complicated; however, the observation that the morning dew has a large effect on the total current flow [3, 16, 20-22], and the observation that potential induced degradation is seen mostly but not exclusively on the perimeter cells [38-41] confirms that glass surface conduction is the dominant lateral conduction pathway.

As discussed earlier and in other publications [3, 13], the current flow at the AR coating is complicated because it is much more resistive than the polymer which allows for charge build-up, but also for the leakage current to flow to the gridlines where electrochemical reactions occur causing conversion of SiN_xO_y into Na_2SiO_3. For simplicity however, we are modeling our test cells, Figure 13, mostly as 1-D capacitors.

For a capacitor the capacitance (C) is given by,

$$\mathrm{C} = \varepsilon_\mathrm{r}\varepsilon_\mathrm{o}\frac{\mathrm{A}}{\mathrm{d}} \quad Equation\ 6,$$

where A is the area, d is the distance through the electrical insulator, ε_o is the permittivity of free space, and ε_r is the relative permittivity of the insulator, Table 4. The cell can be thought of as a series of capacitors each in parallel to resistors which allows leakage across the capacitors. However, this cannot be modeled as a simple series of capacitor/resistor pairs because the "capacitors" are composed of shared charge located at an interface. Thus, it is more appropriate to model the charge accumulation at the outer glass (Q_G), Glass/polymer (Q_P), Polymer/AR coating (Q_{AR}), and the cell to AR coating (Q_C) represented as areal charge densities.

Table 3. Test sample modeling dimensions and characteristics

Component	Symbol	Size
Glass Thickness	dG	3.2 mm
Encapsulant Thickness	dE	0.46 mm
AR coating Thickness	dAR	200 nm
Glass Relative Permittivity	εrG	7.75
Encapsulant Relative Permittivity	εrE	2.3
Silica	εrSiO2	3.8
Si3N4	εrSiN	7.5
AR coating Relative Permittivity	εrAR	5

Table 4. Test sample modeling dimensions and characteristics. Permittivity values were obtained as estimates from typical literature values. Capacitance calculated according to Equation 6,. Resistance calculated using parameters from Table 3.

Component	Relative Permittivity	Thickness	Layer Capacitance (nF)	Resistance at 23°C and 50% RH (Ω)
Glass	7.75	3.2 mm	0.055	$7.7\cdot10^{11}$
AR Coating	5	200 nm	570	Unknown
Silica	3.8			
Si_3N_4	7.5			
EVA	2.3	0.46 mm	0.11	$1.7\cdot10^{14}$
POE				$1.1\cdot10^{16}$

For a deployed module at a positive charge there can be a a net charge on it with current flow from the center of the module to the grounded frame. It isn't until one draws an imaginary boundary around enough of the system that the net charge will be zero. For our test sample coupons we assume that the interfaces are infinite planes with one side electrically grounded. Here charge will accumulate at the various interfaces such that the sum of the charge is equal to zero,

$$Q_G + Q_P + Q_{AR} + Q_C = 0 \;\; Equation\ 7.$$

At steady state this charge will be in the form of electrons or holes in the cell and primarily ionic species in the other layers of the same net but opposite charge.

Making an assumption that the charge is effectively in the form of an infinite plane, then the electric field, which is the force (*F*) exerted on a particle with a charge (*q*), in each layer is given by,

$$\vec{E} = \frac{F}{q} = \frac{V}{t} = \frac{Q_2 - Q_1}{2 \cdot \varepsilon_r \varepsilon_o}, \text{ Equation 8.}$$

where *V* is the voltage difference between the two interfaces, *t* is the distance between the two plates, and the *Q*s are the charge densities on the opposite sides of the two interfaces but not necessarily at the interfaces. For sets of infinite planes of charge with a net zero charge, the electric field outside of the furthest plane is zero. For a typical capacitor the positive and negative charge on the two capacitors are equal and opposite allowing the factor of ½ and one of the *Q*s to be eliminated in a similar equation. Electric fields obey the law of superposition meaning that the composite electric field from two or more sets of charge pairs can simply be summed up. Because the negative charge on the cells must be balanced by an equal positive charge at the relevant interfaces, the contribution to the total electric field is just the ratio of that charge to the permittivity. With this, the electric field in the glass (E_G), polymer (E_P), and AR (E_{AR}) layers are given by:

$$E_G = \frac{Q_G}{\varepsilon_G \varepsilon_o}, \; E_p = \frac{Q_G + Q_P}{\varepsilon_P \varepsilon_o}, and \; E_{AR} = \frac{Q_G + Q_P + Q_{AR}}{\varepsilon_{AR} \varepsilon_o}, \text{ Equation 9.}$$

where the subscripts *G*, *P*, and *AR* refer to the properties of the glass, polymer or anti-reflective coating, respectively. The product of the various electric fields and the distance results in a voltage drop. This static charge serves to counteract the flow of charge through the cell layers. The sum total of the static voltage is given by:

$$V = \frac{t_G Q_G}{\varepsilon_G \varepsilon_o} + \frac{t_P (Q_G + Q_P)}{\varepsilon_P \varepsilon_o} + \frac{t_{AR} (Q_G + Q_P + Q_{AR})}{\varepsilon_{AR} \varepsilon_o} = \frac{Q_G}{C_G} + \frac{(Q_G + Q_P)}{C_P} + \frac{(Q_G + Q_P + Q_{AR})}{C_{AR}},$$

Equation 10.

This total voltage can be expressed in terms of the ratio of the net charge on both sides (not just charge immediately on the surface) to the capacitance of the various layers. The resistivity of the glass is several orders of magnitude lower than the polymer which results in $Q_G << Q_P$ because only a very small voltage drop across the glass will reduce the charge differential and the charge will have a much more difficult time traversing the polymer. Therfore the first term in Equation 6 is essentially negligible at steady state and there is an insignificant amount of charge at the outer glass interface, Q_G. At steady state, the only significant voltage across the glass is associated with the flow of current.

Glass Resistivity Estimation

Prior to turning on the voltage, it can be assumed that essentially all the charge has been dissipated. When the voltage is turned on, there will be some charge build-up on the two electrodes associated with the Keithley measuring instrument and the whole sample but this is so fast that its effect is not measureable and may be neglected. The resistance across the glass is much less than across the polymer; therfore, the initial transient response can be expected to function as a simple series RC circuit. Here, the initial current is determined by the ratio *V/R* because an uncharged capacitor acts as an open circuit. As the capacitor charges up, a voltage builds up to oppose the flow of current, leading to an exponential decay in current for a simple RC circuit as,

$$I(t) = \frac{V}{R}\left(1 - e^{-\frac{t}{RC}}\right), \text{ Equation 11.}$$

In our test cells this holds approximately true for short time frames where the equivalent resistor is that of the glass and the short time capacitance (C_o) is given by,

$$C_0 = A\varepsilon_0\left(\frac{\frac{\varepsilon_P\varepsilon_{AR}}{t_P t_{AR}}}{\frac{\varepsilon_P}{t_P}+\frac{\varepsilon_{AR}}{t_{AR}}}\right) \approx A\varepsilon_0\left(\frac{\frac{\varepsilon_P\varepsilon_{AR}}{t_P t_{AR}}}{\frac{\varepsilon_{AR}}{t_{AR}}}\right) = \frac{A\varepsilon_0\varepsilon_P}{t_P} = C_P, \text{ Equation 12.}$$

The thickness of the AR layer is so relatively thin that when looking at the overall capacitance, it can be ignored. For this series RC circuit the logarithm of the initial decay in current flow can be used to estimate the resistance of the glass (R_G) as,

$$R_G = \frac{t}{[\ln(I_o)-\ln(I)]C_o} \approx \frac{t_2-t_1}{[\ln(I_1)-\ln(I_2)]C_P}, \text{ Equation 13}$$

Because it is not possible, with the equipment we used, to measure the current at the instant the measurement begins, we use the first two data points which are at best at 2.6 s and 3.4 s, or for the worst case scenario, of a FC +1000 V without solder run (Table 5), where the first two points were at 46.6 s and 47.5 s. The use of secondary points is theoreticaly valid for a system with just one capacitor and one resistor so long as the charge has not yet built up on the AR-polymer interface. The characteristic time constant for charge build-up on the AR coating is given by $R_p \cdot C_{AR}$ which is approximately $2.52 \cdot 10^{10}\ \Omega \times 5.71 \cdot 10^{-7}$ F = 14,000 s, substantiating the idea that this is not significant at these short timescales.

Table 5. Transient current characteristics of test samples. Data from the first Voltage-On cycle was ignored in these calculations. For most samples, only one measurement was made, but for some duplicate measurements were made and sometimes with different cycle times as indicated.

Cell Type	Solder and Tabbing	Encapsulant	Voltage (V)	Voltage-On Steady State Current (nA)	Voltage-On Cycle Charge (mC)	Voltage-Off Cycle Charge (mC)	Voltage-On Initial Current Measurement at ~2.4 s (nA)	Voltage-Off Initial Current Measurement at ~2.4 s (nA)	Voltage-On Apparent Glass Resistance from Initial Current Measurement, Equation 9 (Ω)	Voltage-Off Apparent Glass Resistance from Initial Current Measurement, Equation 9 (Ω)	Voltage-On Time Constant 1/RC, Equation 11 (1/s)	Voltage-Off Time Constant 1/RC, Equation 11 (1/s)	Voltage-On Glass Volume Resistivity from short time RC slope, Equation 11 (Ω)	Voltage-Off Glass Volume Resistivity from short time RC slope, Equation 11 (Ω)	Comment
BC	NA	EVA	+1000	0.91	0.039	0.00085	6.1	8.7	$1.6 \cdot 10^{11}$	$1.1 \cdot 10^{11}$	5.74	1.52	$5.0 \cdot 10^{10}$	$1.3 \cdot 10^{10}$	Two, 4 h cycle
BC	NA	EVA	+1000	0.95	0.041	0.0012	6.2	8.8	$1.6 \cdot 10^{11}$	$1.1 \cdot 10^{11}$	5.94	1.52	$5.2 \cdot 10^{10}$	$1.3 \cdot 10^{10}$	Two, 5 h cycles
BC	NA	EVA	+1000	3.7	0.16	0.0043	21	21	$4.8 \cdot 10^{10}$	$4.8 \cdot 10^{10}$	2.77	1.41	$2.4 \cdot 10^{10}$	$1.2 \cdot 10^{10}$	
FC	No	EVA	-1000	4.7	0.21	0.0023	32	30	$3.1 \cdot 10^{10}$	$3.3 \cdot 10^{10}$	2.73	1.64	$2.4 \cdot 10^{10}$	$1.4 \cdot 10^{10}$	
FC	No	EVA	+1000	4.7	0.20	0.0013	23	26	$4.4 \cdot 10^{10}$	$3.8 \cdot 10^{10}$	3.46	1.51	$3.0 \cdot 10^{10}$	$1.3 \cdot 10^{10}$	
FC	Yes	EVA	+1000	11	0.75	0.00024	52	9.4	$1.9 \cdot 10^{10}$	$1.1 \cdot 10^{11}$	6.33	1.72	$5.5 \cdot 10^{10}$	$1.5 \cdot 10^{10}$	Three cycles
FC	Yes	EVA	-1000	7.3	0.39	0.0024	39	34	$2.6 \cdot 10^{10}$	$2.9 \cdot 10^{10}$	2.89	1.73	$2.5 \cdot 10^{10}$	$1.5 \cdot 10^{10}$	
FC	Yes	EVA	+1000	20	0.89	0.031	47	29	$2.1 \cdot 10^{10}$	$3.5 \cdot 10^{10}$	3.24	0.83	$2.8 \cdot 10^{10}$	$7.3 \cdot 10^{9}$	
FC	Yes	EVA	+1000	15	0.66	0.0021	35	22	$2.9 \cdot 10^{10}$	$4.5 \cdot 10^{10}$	4.73	1.13	$4.1 \cdot 10^{10}$	$9.9 \cdot 10^{9}$	Three cycles
BC	NA	POE	+1000	1.5	0.090	0.00041	22	21	$4.6 \cdot 10^{10}$	$4.8 \cdot 10^{10}$	2.54	1.21	$2.2 \cdot 10^{10}$	$1.1 \cdot 10^{10}$	
FC	NA	POE	+1000	NA	NA	0.00026	53	22	$1.9 \cdot 10^{10}$	$4.5 \cdot 10^{10}$	3.21	NA	$2.8 \cdot 10^{10}$	NA	Inconsistent Data

Charge accumulation in the interior layers of the samples is not expected to affect these initial measurements according to Equation 11. This assumption is validated by the consistency of these time constant measurements in Table 5 for all cell and encapsulant configurations when comparing the voltage-on transitions or voltage-off transitions to each other but not when comparing voltage-on to voltage-off transitions. The independence from the cell geometry and encapsulant type indicates we are indeed measuring the effects of the initial charging at the glass to polymer interface. The voltage-off transient current time scale is about 1.4 s as opposed to 4.0 s which cannot be explained by a change in the capacitance of the encapsulant but must therefore indicate the glass resistance after charging. This increase in the glass resistance by 2.9× upon voltage exposure may help to explain some of the observed higher current in modules in the morning [42]. This increase is most likely the result of the depletion of charge carriers in one of the glass surfaces creating a more resistive and purer SiO_2 surface layer.

The glass resistance can also be estimated from the initial current as the ratio of V/I_o, Equation 9. However, the electrometer can only measure the resistance after a finite time of a few seconds making the resistance estimate systematically high with this method. On average this produced resistances that were 59% higher than when using the initial slope in Equation 11. This is consistent with time scales being on the order of 4 s to 1.4 s and the measurements being made a few seconds after the switching of the voltage. We did not see statistically significant differences between the different configurations. Similarly, we did not see a statistically significantly different difference between R_G measured from the initial voltage-on or from the voltage-off current measurements. This contrasts with the estimate made using Equation 11 which did show differences, but the standard deviation was 36% and 20% for On vs Off measurements (Equation 11) as opposed to 98% and 57% for On vs Off measurements (first measured current). We believe the inability to find a difference here is related to the experimental variability which could be fixed or mitigated by better sampling and statistics, but the decay time method is clearly the preferred method to do this.

The simplistic 1-D models underlying Equations 8, 9, 10 and 12 have some concerns with some relevant 3-D aspects. In particular the metallization requires another assumption to be applied to this model framework which has some validity concerns because the spacing is of a relevant width compared to the encapsulant thickness. In the FC cells, the metallization also traverses the AR coating and penetrates into the polymer layer. The relevant thickness for the glass, encapsulant, and AR coating are approximately d_G=3.2 mm, d_E=0.46 mm, and d_{AR}=~200 Å, respectively (Table 4). In these cells, the metallization spacing was ~1.16 mm, the width is about ~0.050 mm and the height is around ~0.040 mm.

Earlier [4, 13] we demonstrated that the electrochemical reactions on the cell surface result in the formation of sodium silicates near the gridlines. This indicates that the current flows to the AR coating and builds up a charge, with the AR coating acting as a capacitor/insulator. Then some of the current flows laterally to the gridlines. The BC cells have no front side gridlines and have been shown to have pronounced charging effects. In our experiments, it was found that the BC cells had generally lower steady state voltage-on leakage currents, Table 5, indicating the dominance of the pathway of charge flowing through the metallization as opposed to flowing through the AR coating. In Swanson et al. [24], they explain that the presence of light serves to make the AR coating photoconductive which allows the charge to dissipate. This is an electronic mode of charge transfer indicating that there must necessarily be electrochemical reactions

occuring at the AR coating to polymer interface. Noting that the conversion of silicon oxy-nitride to silicates is not reported, the more dominant electrochemical reaction is the splitting of water into either hydroxide or hydronimum ions which does not appear to rapidly corrode the surface. It is likely that the bacicity in the polymer is simply not strong enough and/or hydroxide ions are being converted elsewhere to oxygen and water to partially neutralize the chemistry. In the BC cells the lower currents (Table 5) also indicates that these electrochemical reactions are less pronounced relative to the FC cells. We assume these electrochemical reactions are much more easily catalyzed on the metallization as opposed to the AR coating. Thus standard front metallization cells would be expected to be in a more corrosive environment (i.e. more extreme high or low effective pH).

Simplified Schematic for Current Flow Modeling

A rough schematic of the current flow is shown in Figure 15. Here the lateral current flow, illustrated as flowing from the AR coating to the metallization can be assumed to dominate over the current flow through the AR coating such that in a modeling effort, flow through the AR coating can be essentially ignored. Because of the relatively small height and width of the metallization compared to the thickness of the encapsulant and as we will see, the variability in the resistance values, this penetration of tabbing into the the encapsulant was ignored. The thickness and spacing of the metallization are of the same order of magnitude making the 2-D nature of the electric field still impact current flow to the metallization.

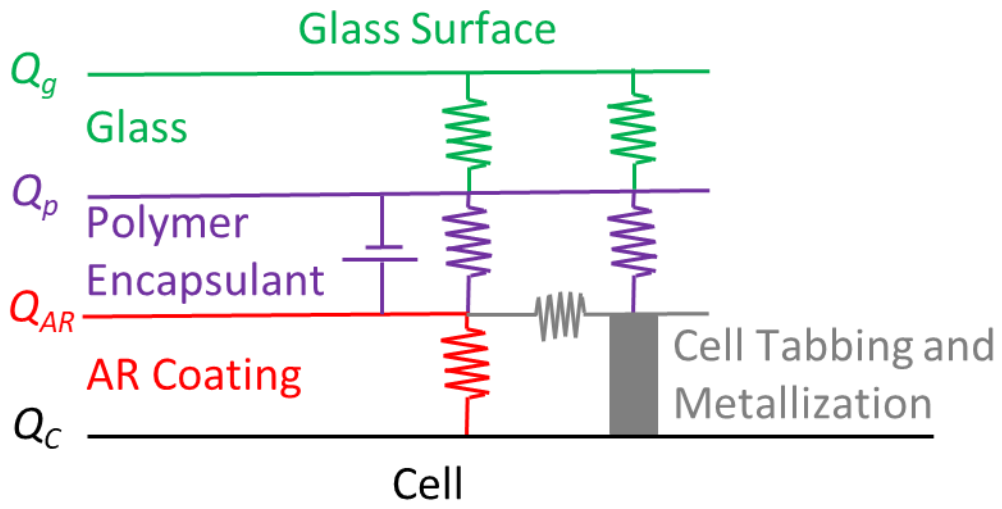

Figure 15. Schematic of electrical circuit for conduction of current through the cell. This model is not intended to be an exact representation but just to illustrate the primary charge sources and effective pathways.

To evaluate the current flow to the metallization in the FC cells, we must consider the voltage above the AR coating and on the glass to polymer surface. In Table 5 we show the steady state current in the voltage-on state which for 50.8 cm × 50.8 cm cell test samples averages to $1.05 \cdot 10^{-8}$ A and $1.75 \cdot 10^{-9}$ A for FC and BC respectively. Thus a rough estimate would be that about $1/6^{th}$ of the current is flowing through the AR coating in the FC cells. When exposed to light, some increase in the photoconductivity of the AR coating would be expected to reduce this ratio of current pathways. To estimate the maximum voltage drop across the AR coating in the FC cells one could assume a maximum charge build-up in the center of the cell then lateral current flow across the AR surface with charge density decreasing to a value, that is still non-zero, at the metallization interface. There is a problem with making this estimate of the relative current flow through the AR coating and through the metallization, we don't have a way to estimate the amount of charge build-up around the gridlines. When the voltage is turned off, $5.68 \cdot 10^{-6}$ C and $1.68 \cdot 10^{-6}$ C are dissipated for the FC and BC cells respectively. However the standard deviaiton for these measurements is between 103% and 198% making this difference insignificant. This can be interpreted as the presence of the AR coating does not affect the charge build-up, that there are relevant differences in the AR coatings (from different manufacturers), and/or that the transient behavior and chemistry is dramatically different.

The schematic shown in Figure 15 can be simplified for the BC cells as a removal of the metallization making it a 1-D current flow model. For FC cells, the presence of gridlines does not seem to have an effect on charging that is larger than many of the other variabilities in the current flow and can be thought of as an uncertainty in the charge path length where it is effectively about 50% longer at most. Therfore, for the purposes of more rigorous modeling to elucidate more information about current flow, we will assume the FC cells to be primarily 1-D in nature.

Measurements of Current Flow from a Frame

In the experiment using a copper foil to represent a frame, Figure 14, when EVA was used the difference between the applied voltage or the cell type was irrelevant, Figure 16. But for the PO encapsulant there was a significant difference between the FC and BC cells. It is known that Na^+ is a significant contributor to PID and that EVA provides better conductivity to Na^+ than does PO, even when the overall conductivity of the two polymers is comparable [33, 35, 36]. The difference, Figure 16, is likely due to the presence of metallization, but the observation that both positive and negative biases had similar conductivity for the BC cells indicates that this phenomena is not just attributable to the presence of Na^+. There must be other ions that have conductivities that are sensitive to polymer type and experience electrochemical interactions with the metallization. We hypothesize that the metallization allows for electrochemical reactions to occur more easily and that with the BC cells there is a build up of ions resisting the flow of current.

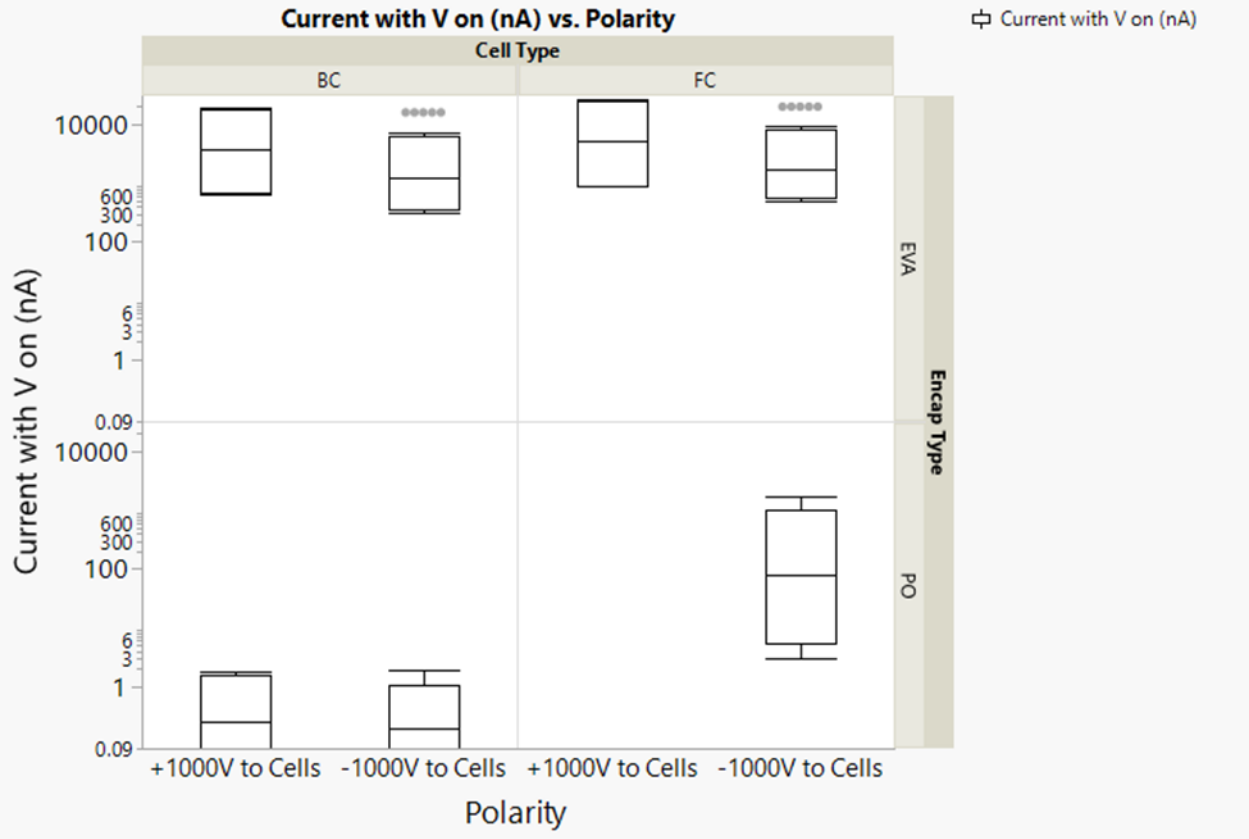

Figure 16. Steady state voltage-on current for minimodules with a metal foil frame under applied voltage to the cell. The data point for FC cells at +1000 V in PO was simply not taken.

Effects of Multiple Charge Carrier Types

For the 1-D test samples, Figure 13, we typically ran the charge/discharge cycle 5 times for a length of time of 12 h for both the Voltage-On and Voltage-Off phase of each cycle to duplicate a typical diurnal cycle. The first charge cycle typically differed from the rest, but good consistency with the remaining cycles was typically obtained (Figure 17). For all samples tested, the terminal discharge values were almost always in the upper 10^{-11} A range and the steady state Voltage-On current was between $9 \cdot 10^{-10}$ A and $2.00 \cdot 10^{-8}$ A, Table 5. During charging there is a fast reduction in current leading to a plateau value. Then in the Voltage-Off phase there is an initial fast decay followed by a slower decay at very low currents. This indicates the presence of at least two important species or processes with different time scales. We also assumed that the instrumental response, and the response time for dipole moment reorientation were much faster than the 2.4 s required for the first data point to be recorded and where thus ignored.

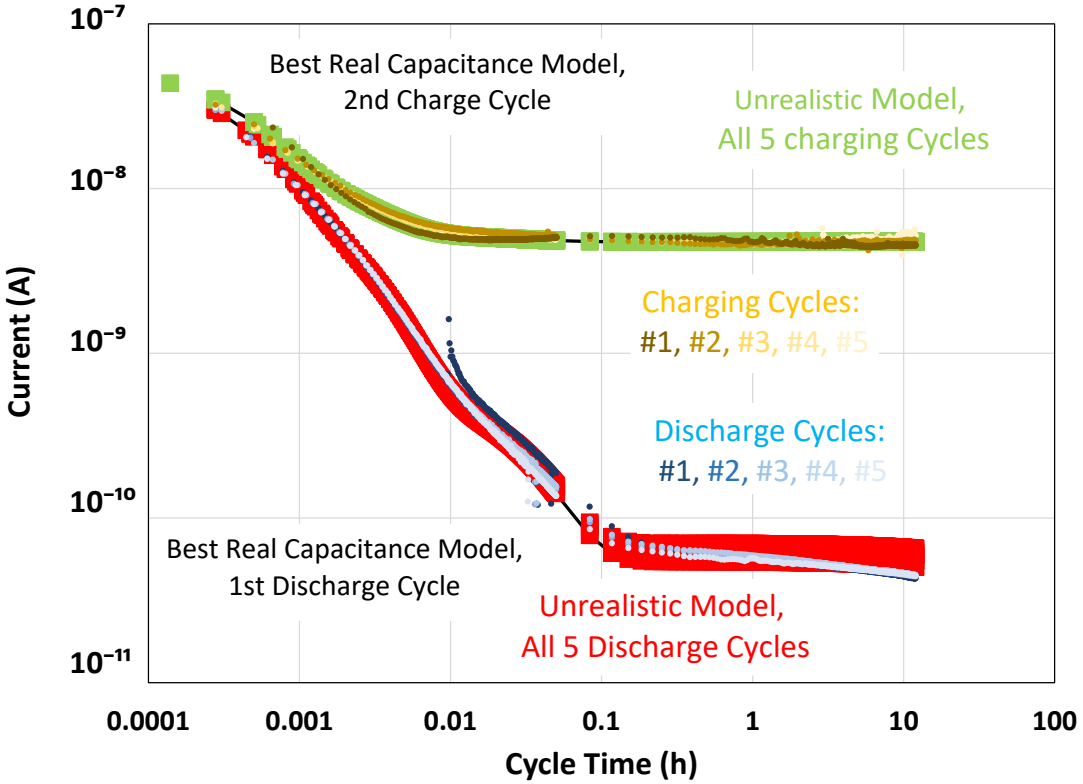

Figure 17. Transient current measurements for an FC cell with solder and EVA. The fit used here (Red and Green markers) required unrealistic capacitance values to work. The parameters for these fits are indicated in Table 5.

As a first attempt at modeling the complete current flow, the sample is modeled with an electric field across the glass, polymer and AR layers according to Equations 9 and 10. This is essentially using the capacitance of these layers in conjunctions with charge build-up at each of the interfaces. Then current is allowed to pass through the layers with the glass being modeled as having a constant resistance. However the shape of the discharge curves, e.g. Figure 17, clearly indicate the transport of at least two important species or processes with different time scales as seen by the dramatic change in the slope. This is relevant at time frames greater than 0.1 h (360 s), but the glass charging process has a characteristic time on the order of about 1.4 s and no indication of secondary processes. Thus the location of this multiplicity of charge carrier processes is predominantly associated with the polymer layer. To model this, we modeled three different species with a different mobility ($1/R_{P1}$, $1/R_{P2}$, and $1/R_{P3}$) such that the electric field across the polymer is calculated according to Equation 9 from which the charge transfer is calculated and separately accumulated at the polymer AR coating interface for the three species separately. Here it should be noted, that the build up of charged species can be from the production of positive and negative species with one leaving, or equally from the influx of either a positive or negative species. For this analysis, it is assumed that there is an infinte supply of charged species. This is true for species coming from the glass or for those derived from the splitting of water. In Equation 9, the total electric field is calculated from the sum of the contributions from the various species. Furthermore, the driving force for the loss of a given species at the polymer-AR coating interface (R_{L1}, R_{L2}, and R_{L3}) is proportional to the amount of charge accumulation of that species and the voltage from there to the cell. Again, the voltage is

determined from the sum of the electric charge and applied to each charged species separately with a different loss factor. But when one accounts for both these factors, the leakage current is just proportional to the concentration of the particular charged species. This loss of charge carrier is either by migration to the gridlines or through the AR coating and does not differentiate between electronic flow through the AR coating with electrochemical reactions at the interface or lateral movement to the gridlines where an electrochemical reaction can happen according to one of the scenarios in Table 2.

If one fixes the capacitance across the glass as estimated in Table 4, and uses the value for glass resistance (Table 5) as the average from the voltage-on and voltage-off slopes according to Equation 9, the other parameters, Table 5, can be adjusted to yield a reasonable representation of the curves in Figure 17, (red and green markers). The leakage current resistance values in Table 6 have units of [Ω·C] because the leakage rate of a particular charge carrier in this model is related to the amount of it present. With a remaining unrealistic value for the capacitance of the AR coating, one can obtain a reasonble fit to the data. It takes two different species in the charging part of the cycle to get the curve to match and a third one, which is unnoticeable in the charging cycle, to get the long term discharge characteristics.

Table 6. Parameters for current leakage modeling attempts in Figure 17. Parameters are determined either empirically, from measurements (Table 5), or from typical material parameters (Table 4).

Configuration Description	Rg	Cp	Rp1	RL1	CAR	Rp2	RL2	Rp3	RL3
	(Ω)	(nF)	(Ω)	(Ω·C)	(nF)	(Ω)	(Ω·C)	(Ω)	(Ω·C)
FCC, -1000V, EVA No Tabbing, Unrealistic Capacitance	$1.80\cdot10^{10}$	0.114	$5.50\cdot10^{10}$	$5.70\cdot10^{10}$	0.40	$9.00\cdot10^{11}$	$2.70\cdot10^{11}$	$2.00\cdot10^{16}$	$1.50\cdot10^{15}$
FCC, -1000V, EVA No Tabbing, Realistic Capacitance.	$1.80\cdot10^{10}$	0.114	$7.00\cdot10^{10}$	$5.00\cdot10^{10}$	57100	$2.00\cdot10^{13}$	$1.50\cdot10^{11}$	$1.50\cdot10^{17}$	$1.74\cdot10^{15}$

The movement of minute amounts of charge will not affect the permittivity of the various components or the capacitance of that layer, Equation 6. As demonstrated earlier, the high resistance of the polymer relative to the glass requires the initial part of the charging curve to be dictated by the current flow through the polymer. Until a counter acting voltage is being built up on the AR coating, or the current flow has decreased to near the steady state where significant current is traversing the polymer, the slope on a semi-log curve cannot deviate from a straight line, Figure 18A. Because the AR coating capacitance is about 5000 × larger than the polymer capacitance, and because flow to it through the polymer is orders of magnitude smaller than flow through the glass, a counter acting electric field cannot be produced in the AR coating till much longer time scales. With this model, it is not possible to match up the slope of the charging curve at both the initial times and at intermediate times prior to approaching steady state with a constant resistance in the glass. Therefore, on time-scales of around 30 seconds, the resistance in the glass must be increasing during charging. Because the modeled steady state current is about 2.4 × higher than the measured current in Figure 18A, the glass resistance must be increasing quickly. Then upon removal of voltage the resistance reversibly decreases by about 2.4 ×.

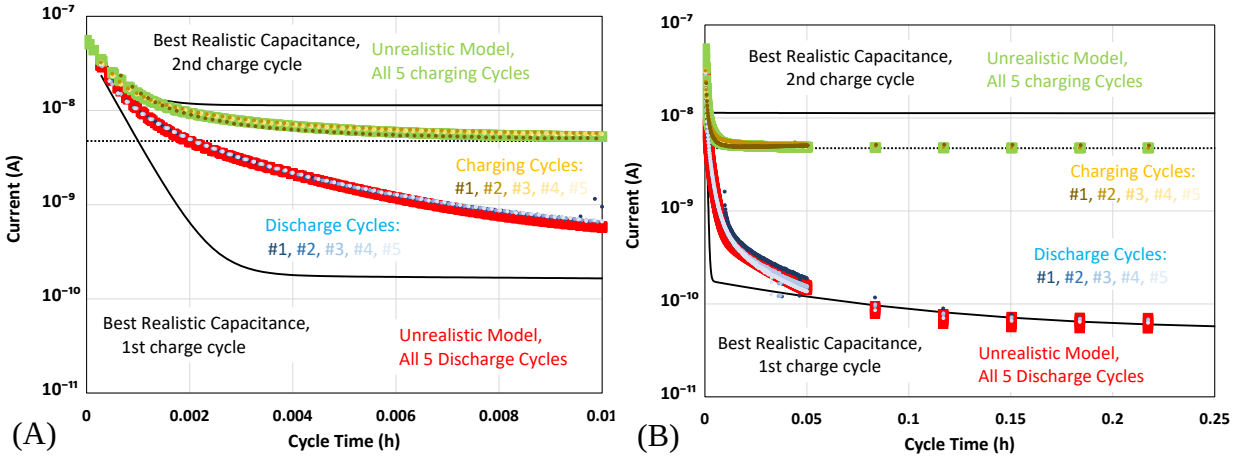

Figure 18. Transient current measurements for a FC cell with solder and EVA. The fit used here (Red and Green markers) required unrealistic capacitance values to work. Shown on a semi-log plot with different time scales to accentuate the appearance of different transient current time scales.

The leakage current clearly shows three distinct time scales for current flow, >0.4 h, 0.4 h to 0.1 h and <0.1 h, Figure 17 and Figure 18. At short times, the leakage current is necessarily higher than predicted because it is still governed by the resistance of the glass. Even if during discharge the model uses lower glass resistance, as predicted by the initial slope, there isn't enough current to match the measured current. If parameters are changed to produce more charge storage from the more mobile charge in the polymer then it doesn't decay to negligible time scales after 0.1 h as measured. Clearly there are other forces or changes in the relevant parameters. Similar curves and similar difficulties were seen in most of the other samples. The only exceptions to this are discussed in the next section. The simple capacitance and constant resistance models just can't explain this data set. As the cell discharges, the resistance to current increases or alternatively, the driving force decreases dramatically through other driving forces.

Effects of Chemical Concentration Gradients

The resistance in the glass goes up as a function of charging which can easily be explained by the formation of resistive layers depleted from alkali elements. This can happen despite an essentially infinite source of ions in the glass. However, when the voltage is removed, the initial current flow is higher and the resistance of the glass from RC measurements is lower than in the voltage on transition. This indicates the presence of additional driving forces for current flow which we believe are due to chemical potential effects. The Nerst equation explains how the activitiy (or chemical potential) of a species is related to the voltage potential in an electrochemical cell. Because the oxidative and reductive activity (a_{Ox} or a_{Red}) is affected by concentration, the depletion of ions in the glass surface layer produces a voltage driving the system towards equilibrium as,

$$V = \frac{RT}{F}\ln\left(\frac{a_{Ox}}{a_{Red}}\right) = \frac{RT}{F}\ln\left(\frac{[Ion\ Concentration\ Electrode\ \#1]}{[Ion\ Concentration\ Electrode\ \#2]}\right)\ Equation\ 14,$$

where R is the universal gas constant T is temperature in Kelvin and F is the Faraday constant. In the context of a PV cell, this could be exemplified as $[OH^-]$ which would drive a water splitting

reaction at the two electrodes producing O_2 and H_3O^+ at one electrode and H_2 and OH^- at another to equilibrate the relative hydroxyl concentration, [OH^-]. Similarly, any of the other electrochemical reactions in Table 2 could be important. Because of this, when the voltage is turned off, there is an additional driving force for current flow resulting from the gradient in ion concentration in the glass. When considering the time scale from an RC current this would manifest as an apparently higher leakage current or lower resistance as was seen.

Conversely in the polymer encapsulant (middle time-scales, Figure 17 and Figure 18), the initial current drops off more slowly than one would expect. The magnitude of the effect cannot be explained by just a recovery of the higher conductivity in the glass. The product of the glass resistance and the polymer capacitance gives a time-scale of 1.4 s and 4.0 s from the initial voltage-off and voltage-on current decay curves respectively. To see a 95% reduction of the initial current would take between 4 seconds and 12 seconds (0.0011 h and 0.0033 h in Figure 17 and Figure 18). Because the time scale for accumulation of charge at the glass/polymer interface is too fast to explain the current decay characteristics, there must be another source of current that is significant and long lived in the polymer.

An infinite series of different charged species with different decay times and magnitudes discharging through the polymer could be made to fit this decay curve. Such a model is purely empirical and thus not useful for understanding the underlying physics. It also implies that there is not a single or even a few species that could be used to simply explain the curve. Attempts were made with three moving charged species, but this could not be used to predict the curve especially when one must acknowledge that the bulk of the initial current flux was from charge already located at the glass to polymer interface.

The increase in resistivity upon application of a DC voltage is a well known phenomena in polymers and insulating materials [43, 44]. The polymer is highly depleted of charge carriers at the end of the voltage-on cycles and the glass would have higher concentrations of carriers at one side and lower concentrations at the other with the middle essentially unchanged creating an opposing electric field. Furthermore, Equation 14 describes a restoring voltage due to differences in chemical potential of concentration of ions across the polymer. It is easy to imagine the concentration of these ions differing by orders of magnitude generating substantial voltages especially considering that the charge separation was created using 1000 V. If there was a 100 × difference in ion concentration or equivalently ion activity, this could produce a 0.12 V driving force across the polymer to the grounded metallization or across the glass. This voltage is much smaller than the initial voltages from charge accumulation at the interfaces and with a glass resistivity of around 3.0 10^{10} Ω the chemical potential induced voltage drop across the polymer cannot account for the excess discharge current for up to 0.05 h. But if it was a little higher than 0.12 V it could explain the terminal discharge current. However, in the glass sufficient charge accumulation at the glass polymer interface could explain some of the initial (<0.05 h) excess current flow. Even if the charge at the glass polymer interface was not there, the chemical potential induced voltage across the polymer may help explain the current flow across the glass. Current from an electrochemical potential would look like an initial shunting leakage pathway for this charge to flow past the glass. This added current would dissipate as the charge at the polymer to glass interface, diminishing the relevant chemical potentials. This could be a partial explanation of the persistent higher measured leakage current which is not explained by the simplistic model of Figure 15.

1-Task 3: Relative humidity at the encapsulant/cell interface will be determined. *(M3-10) NREL*

Task Summary: *The diffusion and solubility of moisture in the encapsulants will be determined from transient water vapor transmission data at a range of humidity and T between 5°C and 85°C.*

Task Details: *There is a risk that the solubility may be extremely low limiting the ability to adequately measure the permeation. It is also possible that one of the materials may not be sufficiently Fickian for this measurement technique to work.*

Milestone 3.1: *Determine solubility and diffusivity of moisture in three encapsulants as a function of T and RH.*

1-Task 3 Results:

Films of an EVA, two polyolefins K2-1 and K2-2, and a polydimethyl siloxane were made with thicknesses (*l*) varying between 0.5 mm and 5 mm. The transient water vapor transmission rate (*WVTR*) was measured for the materials a temperature (*T*) between 5°C and 85°C, with the relative humidity (*RH*) varied between 25% and 100%. The diffusivity (*D*), solubility (*S*), and permeability (*P*) of water was determined at each combination of T and RH by fitting to,

$$WVTR = \frac{DS}{l}\left[1 + 2\sum_{n=1}^{\infty}(-1)^n e^{\left(\frac{-Dn^2\pi^2 t}{l^2}\right)}\right], \text{ Equation 15}$$

where *t* is the time since water was introduced. Then the measurements were fit to an Arrhenius function for temperature and a power law function (*x*) for humidity dependence on solubility as,

$$P = P_o \cdot e^{\left(-\frac{Ea_P}{RT}\right)}RH^x = D \cdot S = \left[D_o \cdot e^{\left(-\frac{Ea_D}{RT}\right)}\right]\left[S_o \cdot e^{\left(-\frac{Ea_S}{RT}\right)}RH^x\right] \text{ Equation 16.}$$

where the fitting parameters include prefactors P_o, D_o and S_o, and the activation energies are Ea_P, Ea_D, and Ea_S for permeability, diffusivity, and solubility, respectively. The results for these materials are given in Table 7.

Table 7 Constants used to model the diffusivity, permeability, and solubility of water in accordance with Equation 16.

Material	Diffusivity		Solubility		Permeability		X
	Activation Energy	prefactor	Activation Energy	prefactor	Activation Energy	prefactor	
	(kJ/mol)	(cm^2/s)	(kJ/mol)	(g/cm^3)	(kJ/mol)	($g \cdot mm/m^2/day$)	
EVA-1	37.9	1.74	12.9	0.289	50.7	4.34	1.06
K2-1	42.3	21.8	21.8	0.779	64.7	$1.81 \cdot 10^{11}$	1.10
K2-2	38.9	6.33	24.0	1.54	62.9	$8.44 \cdot 10^{10}$	1.00
Silicone	10.4	0.00166	25.7	9.40	36.1	$1.35 \cdot 10^{8}$	1.05

The resistivity measurements of four encapsulants and a glass sample were fit to a model using the JMP software package and a non-linear regression analysis providing some uncertainty estimates and correlation coefficients for the modeling parameters, Table 1 and Equation 5. The activation energies had typical uncertainties of around 10%, but the humidity coefficient *a*, had an uncertainty between 10 and 100% for the different materials. Within the experimental uncertainty, moisture is linearly soluble with relative humidity. As is typical for silicones, diffusivity and solubility are very weakly activated.

We developed a leakage current model to predict the amount of leakage current expected in the field for different environments. Leakage current is known to have a large dependence on humidity levels because of surface conduction of the glass. As shown in Figure 12, the glass surface resistivity has the highest dependence of resistivity on humidity increasing more than 100-fold going from 5% to 95% RH at a given temperature. In fielded modules, this is known to result in the vast majority of the leakage current occurring in the early morning when dew is on the modules. Because of this a model for module temperature that included radiative cooling to the atmosphere was needed [7]. Also, to account for the time it takes for a module to equilibrate with its environment, a 20 min delay (relative to irradiance) was used in the data. With this, a 2-D histogram of module temperature vs module surface relative humidity can be calculated (Figure 19). Here we see a very large portion of the time above 100% RH when the temperature is cold at night. For Denver Colorado, there is a very significant amount of time spent well above 100% RH, but this occurs primarily when the temperature is at or below zero °C. This should be thought of as a driving force for condensation. Here moisture will be condensing or depositing on the surface releasing some heat preventing the module from actually reaching its equilibrium state. This represents a systematic error in this temperature model, but as we will see there is very little leakage current occurring at these cold conditions.

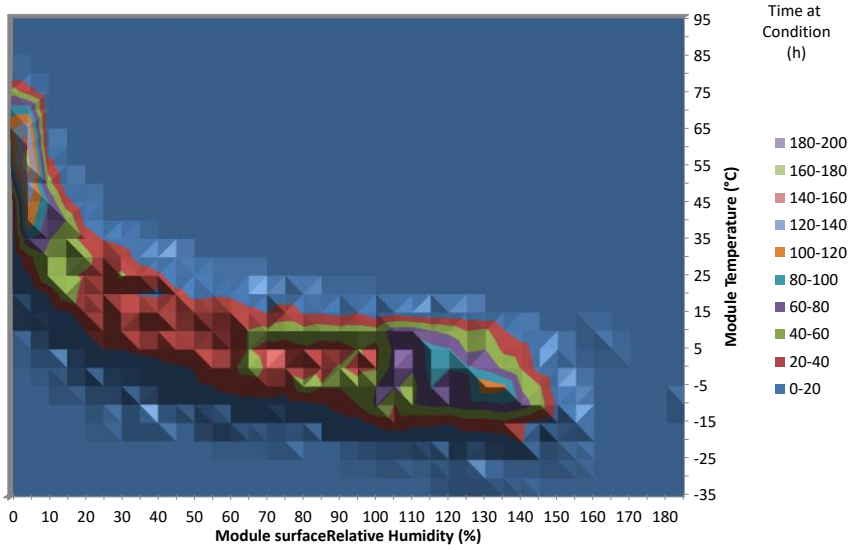

Figure 19. Calculated time at conditions of combinations of module temperature and module surface relative humidity for Denver Colorado for a rack mounted system.

To model the leakage current, we are keenly concerned with times where the voltage is high. We modeled the voltage as having a logarithmic dependence on temperature where at 25°C 1000 W/m² results in a voltage of 1000 V and the voltage decreases 0.5%/°C. A similar 2-D histogram was calculated weighting the time by its voltage/1000 V. As expected, this virtually eliminates the contributions to leakage current that would occur at high humidity when dew or frost is present because this is when the sun is not shining.

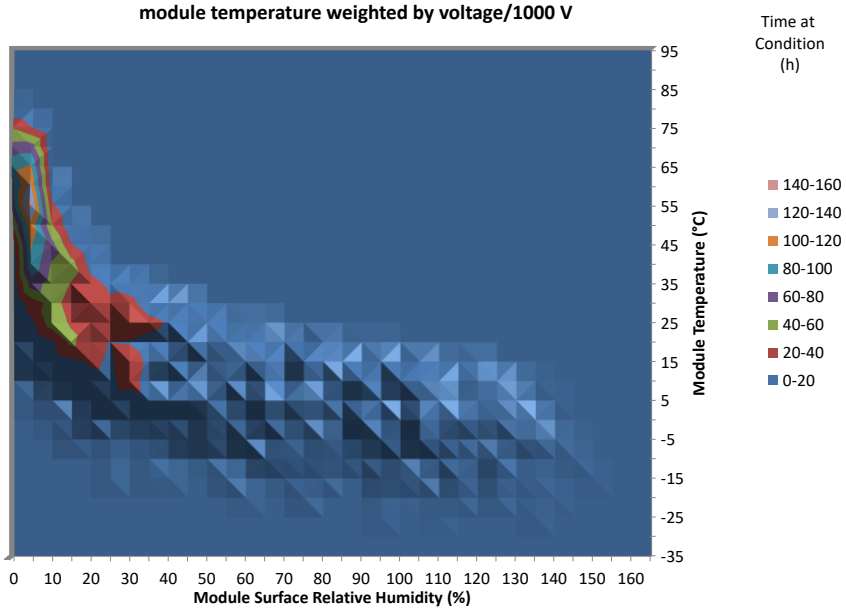

Figure 20. Voltage weighted 2-D histogram of module temperature vs module surface relative humidity.

As shown in Figure 12 and Table 1, the conductivity of the encapsulant is a function of the relative humidity. Glass has a much higher conductivity than typical backsheet materials, therefore electrical conduction out the backside of a module and along the backsheet surface is much less important than the frontside leakage current. Because of this, we are primarily concerned with the moisture content in the front encapsulant film between the cells and the front glass. Here it takes a year or two for the moisture to approach its equilibrium value after which it varies as a function of time and position in the module. Because a module will spend the majority of its time near an equilibrium point, this initial transient period is unimportant.

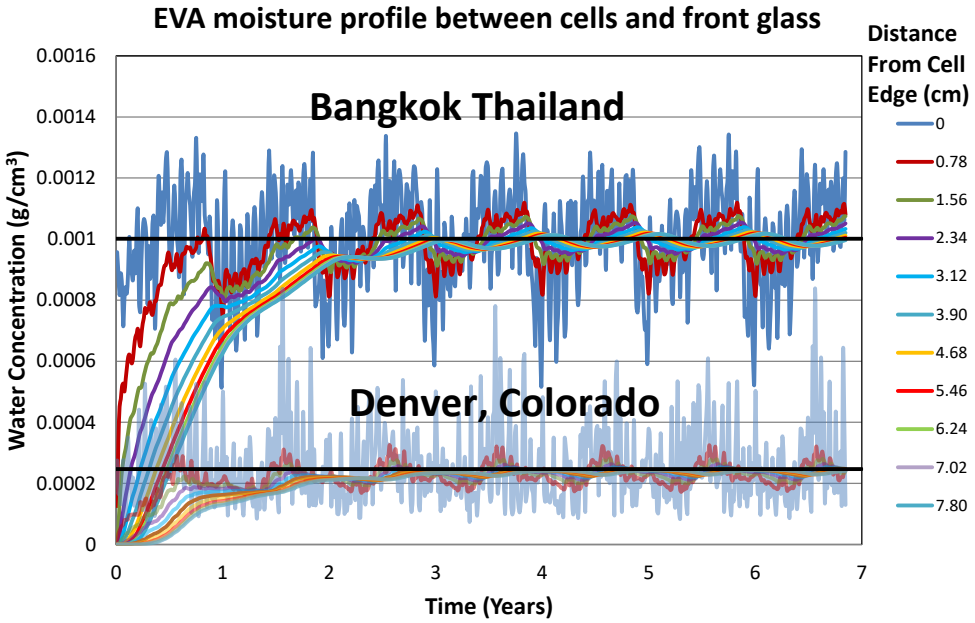

Figure 21. Moisture content in the front encapsulant film layer. The solid black lines are the diffusivity weighted average equilibrium weighted moisture content according to Equation 17.

The equilibrium lines in Figure 21 are the diffusivity (D) weighted average solubility (S_{ave})

$$S_{ave} = \frac{\sum S_{eq} D}{\sum D}$$ Equation 17.

Here S_{eq} is the solubility of water in the encapsulant at equilibrium. In at least the initial modeling efforts, the average water content value will be used instead of the time and spatially varying one. This drastically reduces the necessary computational time. This will allow us to determine which parameters are of the highest importance and focus on those in future iterations.

With a constant absolute humidity, the relative humidity in the front encapsulant layer can be determined as a function of module temperature, Figure 22. Using these parameters for the humidity on the glass surface and in the encapsulant, we are beginning to map out the leakage current response of a module as a function of time.

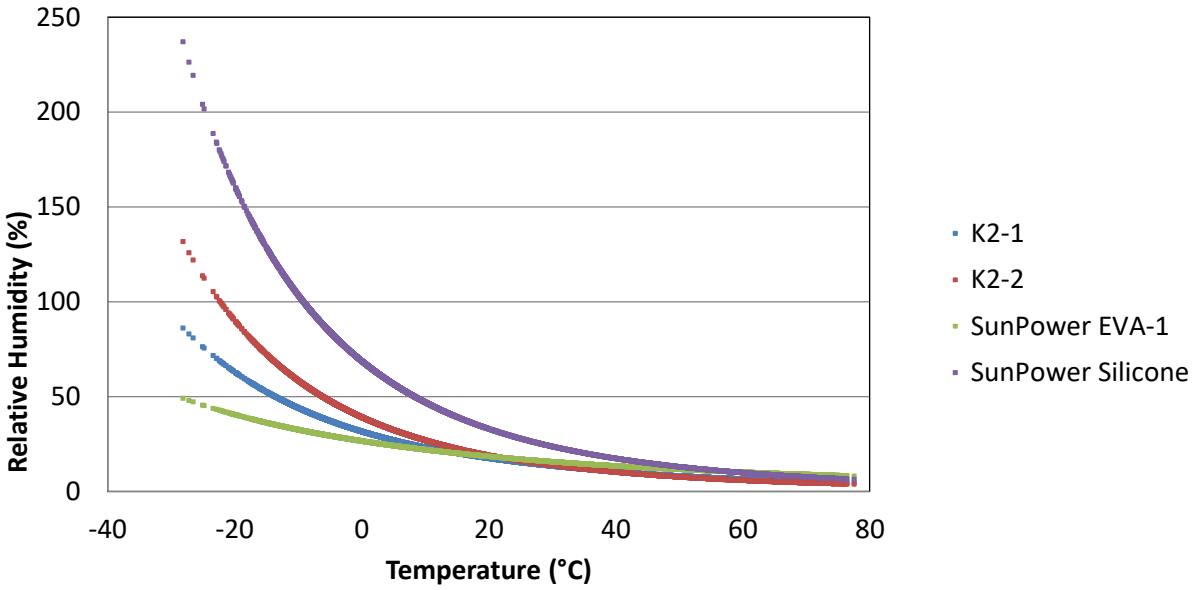

Figure 22. Temperature and humidity curves for the encapsulant on the front side of a module under the assumption of a constant absolute humidity according to Equation 1.

1-Task 4: Field standard and seeded modules. *(M3-M9) SunPower*

Task Summary: *Standard modules and seeded modules will be constructed and placed in the field to allow time for degradation to occur.*

Task Details: *Risk is that the modules will not have any corrosion. The risk mitigation is to construct seeded modules with an increase in T (block airflow and shade cells), RH (delamination), and* I_{leak} *(higher bias voltage).*

1-Task 4 Results:

There were issues with getting all the funding from the DOE for this project. Because of this some of the planned experiments were cut from the project. The main experiment that was not done was the field exposure of seeded modules that were intended to fail. This was chosen to omit because of the long time it takes for field failures to be seen. This time is still long even for seeded modules and it was not very likely to yield useful results before the end of the project.

1-Task 5: Pareto of module field failures. *(Ml-M15) SunPower and NREL*

Task Summary: *Module field failures will be catalogued. RMA (returned modules) will be inspected and examined to determine the root cause of failure. Failure analysis on some modules will be done to determine causes of failures.*

Subtask 5.1: *Compile list of field-aged modules for in-situ testing, indoor non-destructive testing, and destructive testing. (Ml-M6) SunPower and NREL*

Milestone 5.1.1: *List of field-aged (including significantly degraded) modules for analysis.*

Subtask 5.2: *Pareto of module failures. Perform inspection and FA to catalogue failures. (Ml-M6) SunPower and NREL*

Milestone 5.2.1: *Updated pareto of failures of front-contact and back-contact fleets. Completed FA of at least 10 modules from the field. (Ml 5)*

1-Task 5 (Subtasks 5.1 and 5.2) Results:

There were issues with getting all the funding from the DOE for this project. Because of this some of the planned experiments were cut from the project. We were able to find some modules constructed with PVB which showed some clear signs of corrosion and we also found some literature references to PV module corrosion. Unfortunately, because of budgetary constraints, we did not inspect enough samples to form a useful pareto analysis and to do the root cause analysis.

BUDGET PERIOD 2: WORK BREAKDOWN STRUCTURE FOR METALLIZATION CORROSION:

2-Task 1: Determine metallization corrosion mechanism and model for the corrosion type. ***(M16- M25) NREL and SunPower***

Task Summary: *We will perform extensive failure analysis of the coupons in Budget Period 1 and pinpoint the extent and types of corrosion. Models for corrosion rate and ways to measure corrosion will be identified.*

Task Details: *The risk in this task is the identification of the extensive corrosion. Risk mitigation is to input many coupons and carefully monitor the initial appearance and progression of the corrosion. Another risk is that a model is not available for the corrosion type, which can be mitigated by developing a phenomenological model.*

Subtask 1.1: *Identify corrosion type. Analyze coupons with metallization corrosion (Ml 6-M 19) NREL and SunPower*

Milestone 1.1.1: *The corrosion type will be identified for each metal and encapsulant. The specific areas on the cell will also be identified.*

Subtask 1.2: *Determine models and functional forms for the corrosion type. (M 19-M23) NREL and SunPower*

Milestone 1.2.1: *A corrosion functional form and a way to measure the progress of the corrosion will be identified. The corrosion model must include ways to incorporate T, RH, and* I_{leak}*- The information will be disseminated through a published journal article or photovoltaic conference talk.*

2-Task 1 (Subtasks 1.1 and 1.2) Results:

This work is summarized as a complete analysis in the reporting sections of budget period 1 above. It should be noted that the work outlined in budget period 1 actually took place over all three budget periods but it made a more complete story to discuss it all in one section.

2-Task 2: Determine coefficients of the model with corrosion rates measured at different T, RH, and l_{leak}***-*** *(M23-M27) NREL and SunPower*

Task Summary: *Subject coupons and test structures to different environmental conditions (T, RH, and* l_{leak}*). A statistical model must be incorporated to the rate model to calculate the probability that corrosion will occur.*

Task Details: *The risk in this task is an inaccurate corrosion rate model. Risk mitigation is to compare corrosion rates with coupons from Budget Period 1, Task 1. Milestone 2.1. The coefficients in the corrosion rate model will have been determined and correlate well with measured corrosion rates at various conditions in Budget Period 1, Task 1.*

2-Task 2 Results:

There were issues with getting all the funding from the DOE for this project. Because of this some of the planned experiments were cut from the project. The main experiment that was not done was the field exposure of seeded modules intended to fail. This was chosen to omit because of the long time it takes for field failures to be seen. This time is still long even for seeded modules and it was not very likely to yield useful results before the end of the project.

2-Task 3: Merge the complete corrosion rate model with the photovoltaic lifetime models. *(M25- M27) NREL and SunPower*

Task Summary: *The T, RH, and* I_{leak} *dependent corrosion rate model will be input into a photovoltaic lifetime model. Degradation rates will be calculated from the lifetime model.*

Task Details: *The risk in this task is that the model is incorrect. To de-risk the task, the complete corrosion rate PV lifetime model will be compared to the corrosion that has occurred in laboratory samples that have gone through a T/RH cycling.*

Milestone 3.1. *Lifetime model compared to the data from T/RH cycled lab samples and field-aged module (t> 10 yrs). If the model compares well, this information will be disseminated through journal articles and PV conference talks.*

2-Task 3 Results:

There were issues with getting all the funding from the DOE for this project. Because of this some of the planned experiments were cut from the project. The main experiment that was not done was the field exposure of seeded modules intended to fail. This was chosen to omit because of the long time it takes for field failures to be seen. This time is still long even for seeded modules and it was not very likely to yield useful results before the end of the project.

2-Task 4: Characterization of old outdoor modules. *(M20-M27) SunPower*

Task Summary: *Old outdoor modules will be collected. The modules will be examined and characterized to determine any corrosion that may have occurred.*

Task Details: *The risk in this task is that there is no significant corrosion found. To de-risk this, seeded modules will have been placed in the field to induce corrosion.*

2-Task 4 Results:

There were issues with getting all the funding from the DOE for this project. Because of this some of the planned experiments were cut from the project. The main one that was not done was the field exposure of seeded modules intended to fail. This was chosen to omit because of the long time it takes for field failures to be seen. This time is still long even for seeded modules and it was not very likely to yield useful results before the end of the project.

BUDGET PERIOD 3: WORK BREAKDOWN STRUCTURE FOR METALLIZATION CORROSION:

3-Task 1: Characterization of seeded field modules*. (M28 to M31) SunPower*

Task Summary: *The failure analysis of seeded outdoor modules will start. The corrosion rate will be fully characterized in these outdoor modules using the techniques perfected in lab samples.*

Task Details: *The risk in this task is that no corrosion is found. We will de-risk this task by monitoring the modules every six months to make sure that some corrosion has started. From laboratory samples we should get a good sense that these modules will corrode.*

Milestone 1.1: *The corrosion type and rate are measured in the outdoor seeded modules and fielded modules. Include comparisons of impurities in the encapsulant using EDX, mass spectroscopy, gas chromatography, ion chromatography, or other analysis techniques.*

3-Task 1 Results:

There were issues with getting all the funding from the DOE for this project. Because of this some of the planned experiments were cut from the project. The main experiment that was not done was the field exposure of seeded modules intended to fail. This was chosen to omit because of the long time it takes for field failures to be seen. This time is still long even for seeded modules and it was not very likely to yield useful results before the end of the project.

3-Task 2: Accurate corrosion rate PV lifetime model*. (M30 to M35) NREL and SunPower*

Task Summary: *The predictions of the model will be compared to the complete failure analysis of all the fielded modules. Any discrepancies between the model and field data will be examined, and the model will be fixed, possibly with further experimentation.*

Task Details: *The main risk in this task is that the model does not predict outdoor conditions. This risk is mitigated by making sure that the model accurately predicts laboratory samples that have gone through T and RH cycling (Budget Period 2, Task 2).*

Milestone 2.1 *Lifetime model predicts the corrosion from the seeded modules within the environment, measurement, and model uncertainty. The information will be disseminated through journal articles and conference talks.*

3-Task 2 Results:

There were issues with getting all the funding from the DOE for this project. Because of this some of the planned experiments were cut from the project. The main experiment that was not done was the field exposure of seeded modules intended to fail. This was chosen to omit because of the long time it takes for field failures to be seen. This time is still long even for seeded modules and it was not very likely to yield useful results before the end of the project.

3-Task 3: Accelerated tests designed from the model. *(M32 to M39) NREL and SunPower*

Task Summary: *Accelerated tests will be designed from the model and techniques that we have accumulated throughout this study. The predictions from the accelerated tests will be compared to field data.*

Milestone 3.1: *Accelerated tests will be designed to predict corrosion rates in the field. This test will aid the design of more durable metallization. Accelerated tests predict the corrosion from the seeded modules within the environment, measurement, and model uncertainty. The information will be disseminated through journal articles and conference talks.*

3-Task 3 Results:

A module was exposed indoors with ±1000 V applied to the cells as shown in Figure 23. A lot of Na and Ca was found in the tin layer of the back contact fingers of the BCC cells under both positive and negative bias, Figures 24 and 25. This was not expected to be there because Ca and Na are not present in the metallization paste or the solder. No strong accumulation was seen on FC cells, and it was only observed near edges of the BCC cells with glass but was not seen in samples packaged without glass. This indicates it is likely coming from the glass as a leakage current induced effect.

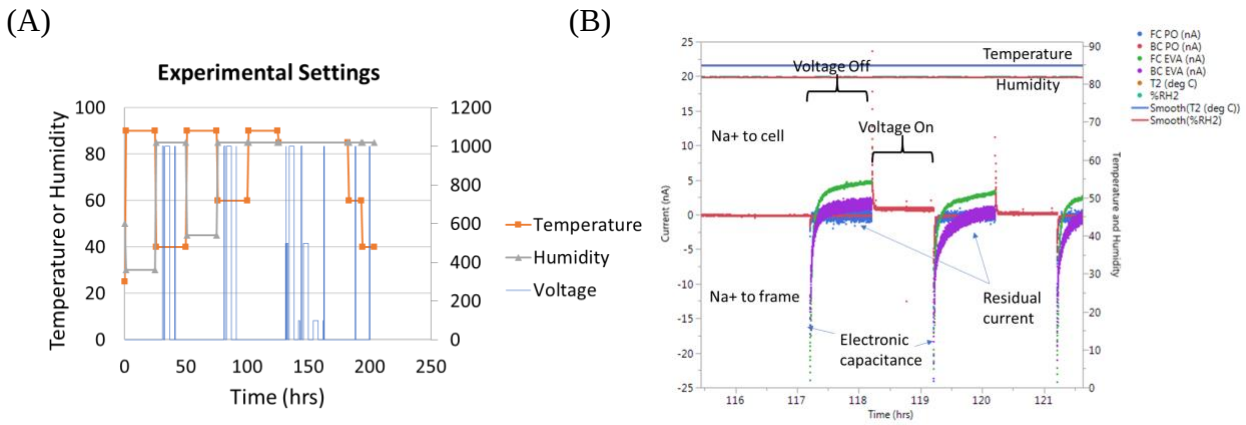

Figure 23. Exposure conditions of minimodule BCC cells.

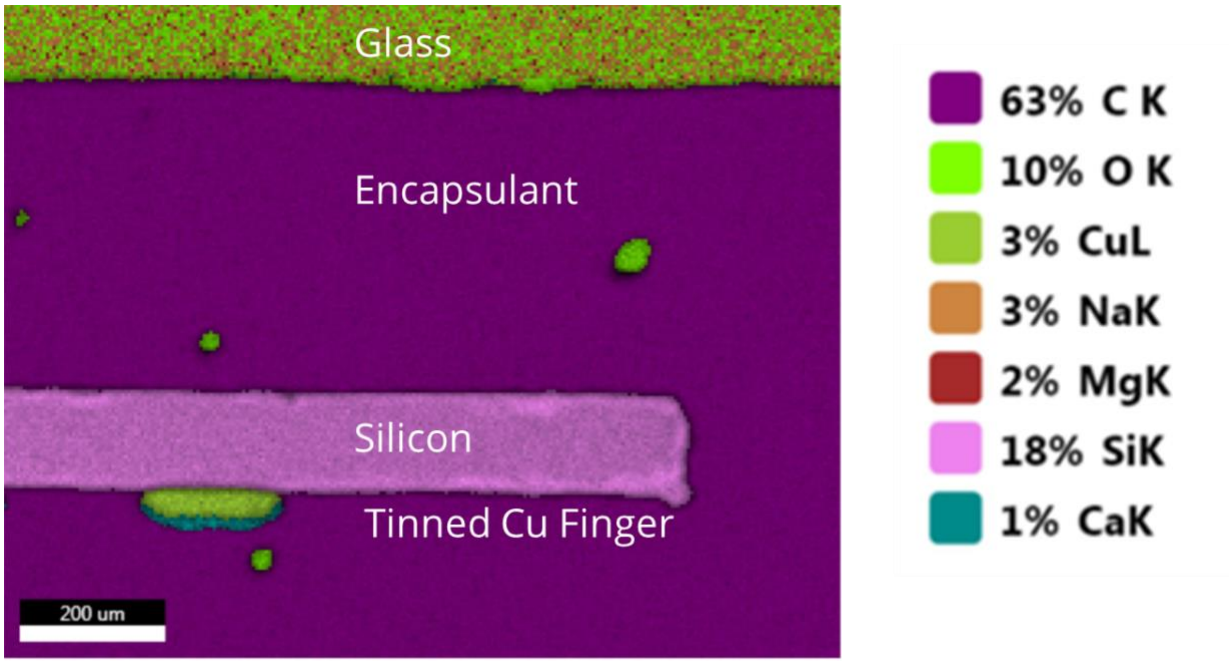

Figure 24. EDS scan of 1000 V positive grounded cell after exposure. Monitoring Ca, Na as primary candidates for electrochemical transport. Exposed as indicated in Figure 23.

(A)

(B)

(C)

Figure 25. Element specific scans from Figure 24.

There were some efforts to make seeded modules where the intent was to promote fast failure of the solder bonds. The stressors here were primarily thermal mechanical stresses applied in accelerated stress chambers as outlined in Figure 26 and Figure 27. Dozens of test structures (coupons) with varying construction were placed in thermal cycling tests with varying speeds. Parametric survival models were fitted to failure data to determine the significant factors for interconnect lifetime. We focused on reduction of profile cycle time rather than changing the low temperature or the high temperature. The actual dwell times of the coupons were reduced relative to the chamber programmed set points due to thermal lag. No current/voltage biasing of samples was used here.

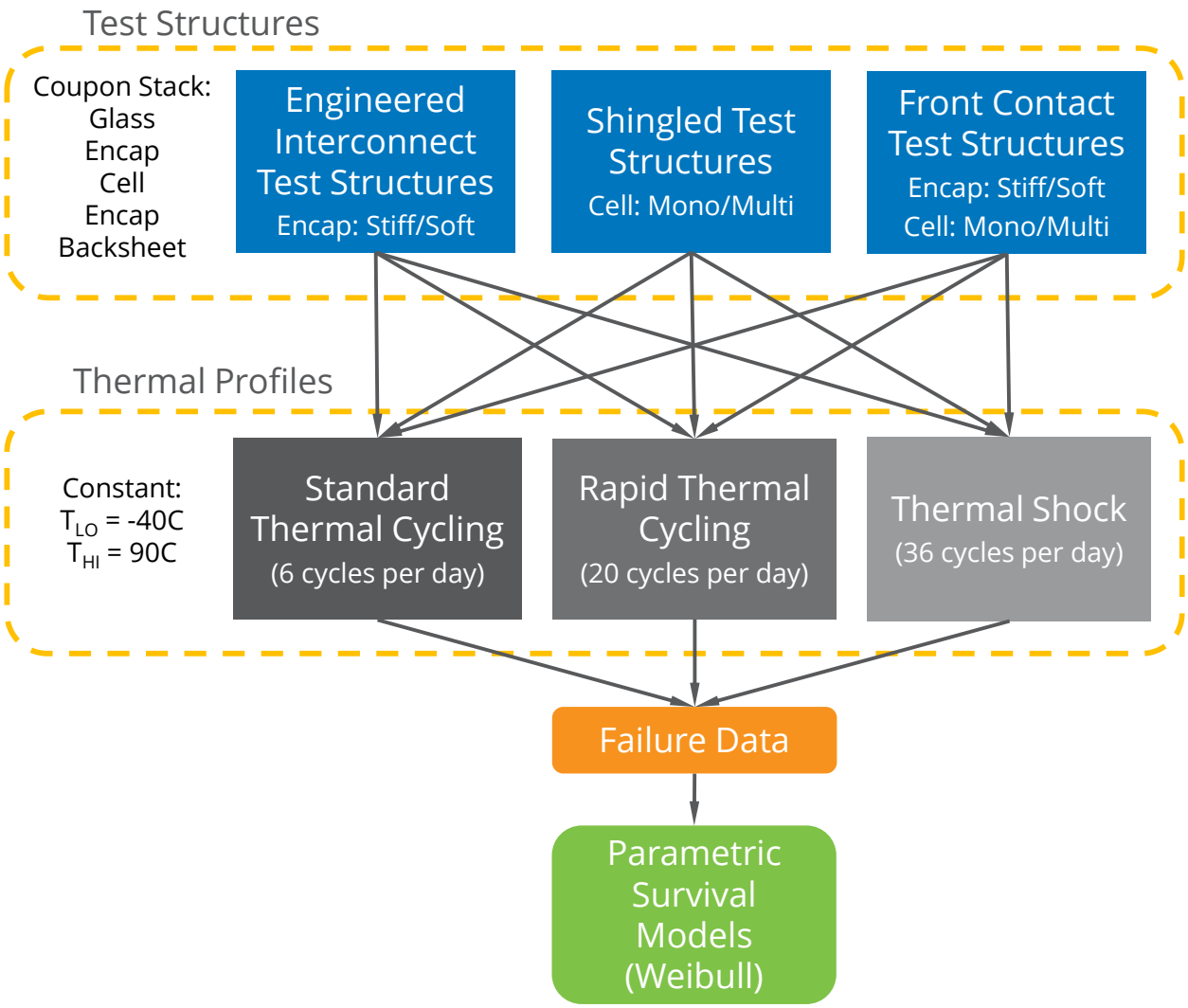

Figure 26. Schematic outline of the thermos-mechanical stress testing.

(A)

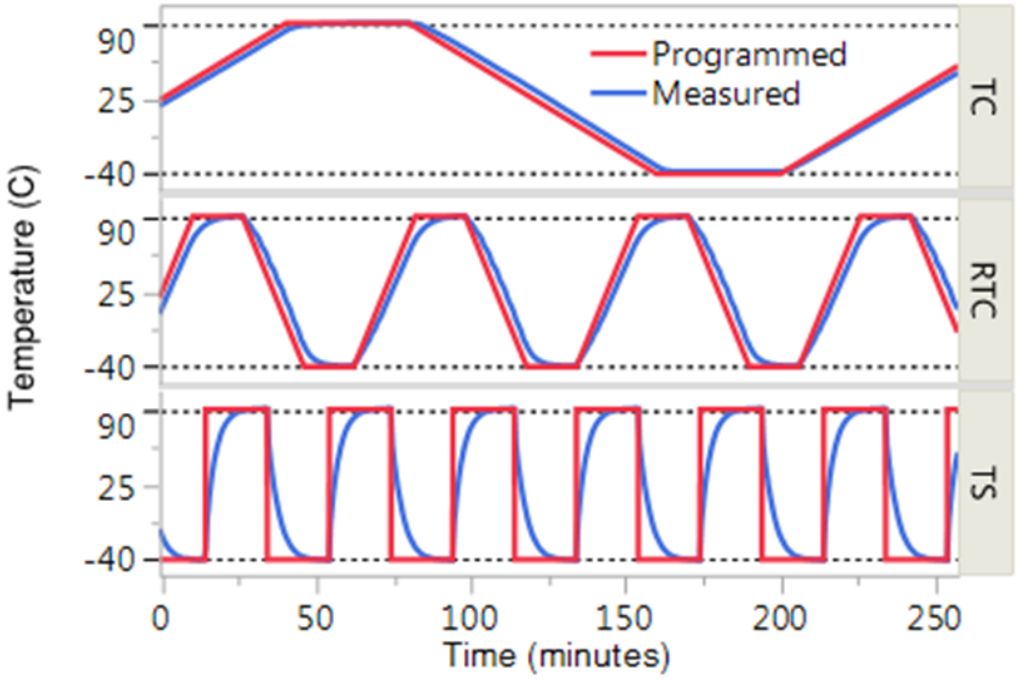

(B)

Profile	Ramp Rate	Dwell Time	Cycles per Day
TC	1.625	40	6
RTC	6.5	16	20
TS	-	20	36

Figure 27. Details for thermal cycling testing exposure.

The test structures used here consisted of three types, Engineered interconnect (EI), Shingles (SH), and Front Contact (FC) as depicted in Figure 28. The EI test structure is set up with wires for in-situ series resistance (Rs) measurements. These were made with 2 encapsulants, 3 chambers and 4 replicates. The SH test structures also can do in-situ Rs measurements and 2 cells in 2 chambers with 2 replicates were made. Lastly, the FC test structures contained active cells from which in-situ dark-IV measurements were made with light-IV measurements at mid read points. Here 2 encapsulants, 2 cells, and 3 chambers with 2 repeats were used. Rs thresholds were applied to each set of degradation data to quantify failure data. Then JMP statistical software was used to fit the parametric survival models to the failure data assuming a Weibull Parametric Survival Model with a Weibull cumulative distribution function,

$$F(x) = 1 - \exp\left[-\left(\frac{n}{\alpha}\right)^{\beta}\right], \text{ Equation 18}$$

where n is the number of cycles, β is and empirically fit shape factor, and α is the characteristic life. An example of how the data was examined to determine these three parameters for the EI samples is given in Figure 29.

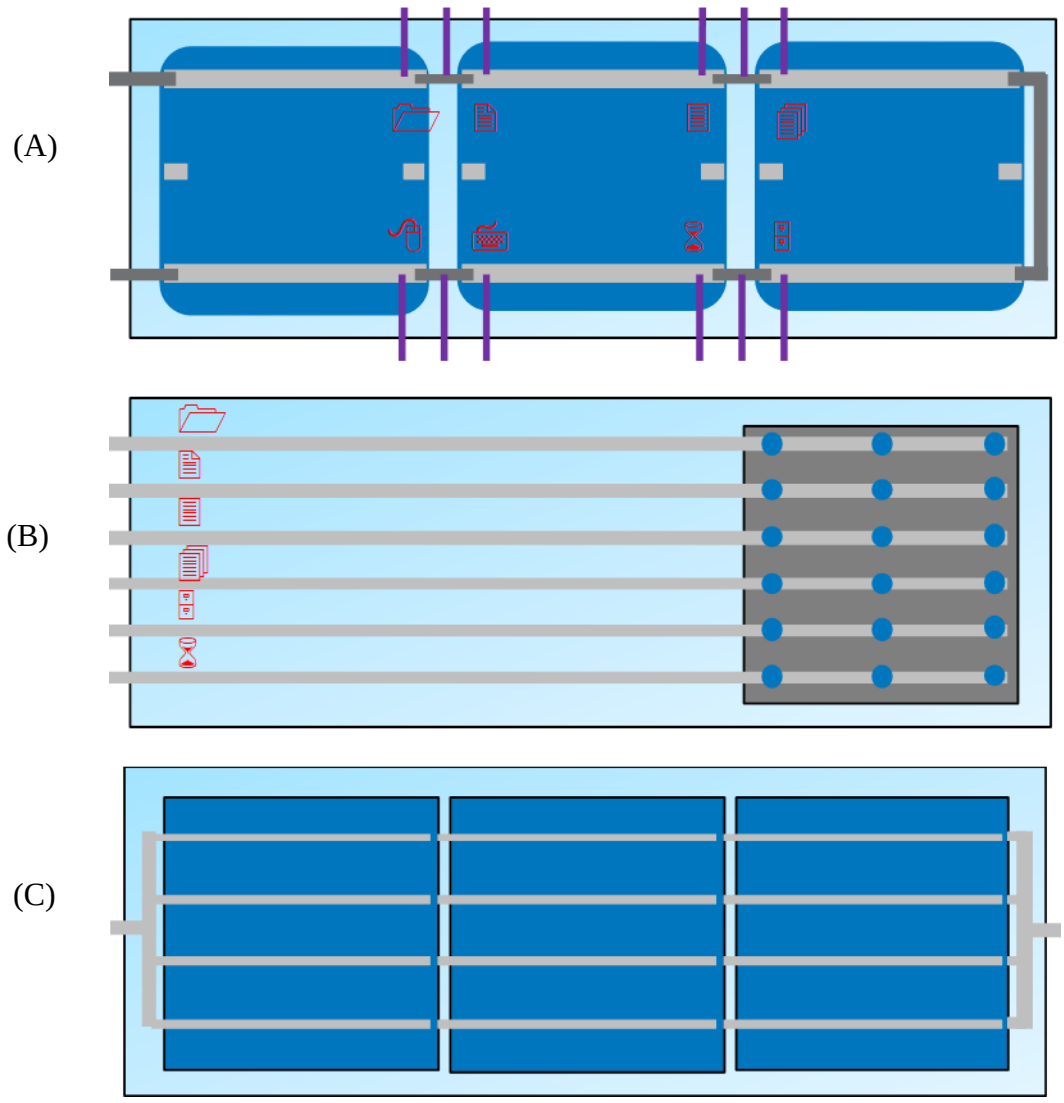

Figure 28. Test structures used in this experiment are specifically designed to apply greater strain to the solder joints. (A) Engineered interconnect (EI) test structures. (B) Shingled (SH) test structures, and (C) Front Contact (FC) test structures.

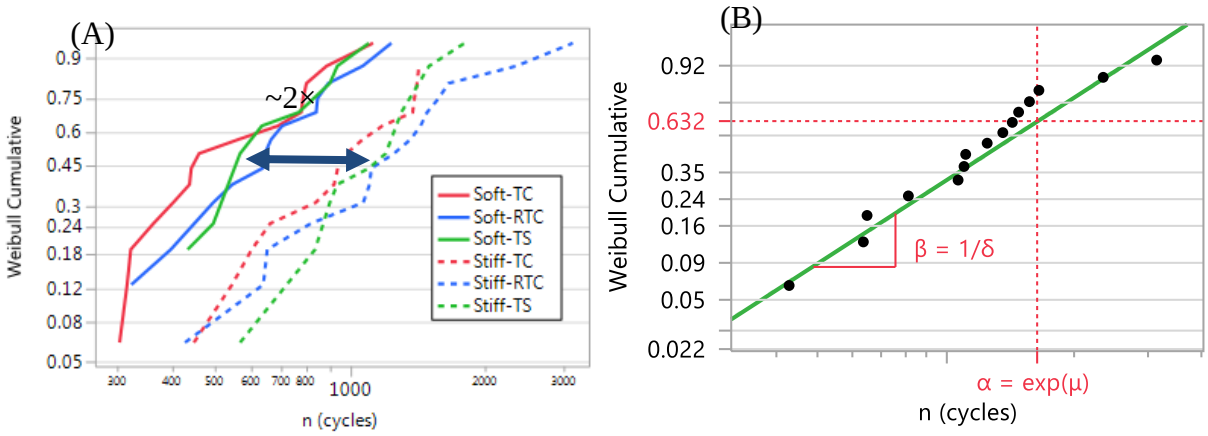

Figure 29. Data for the EI samples. (A) Weibull Failure plot. (B) Log/log plot for extraction of the fit parameters.[45]

In these experiments it was the connecting ribbon that failed in the EI test structure as opposed to the solder bonds in the SH and FC test structures. It was found that the stiffer encapsulant resulted in about a 2× longer expected lifetime for the solder joints. This is most likely because a stiffer encapsulant will cause the cell to be biaxially strained more which minimized the amount of strain that has to be taken up in the wire tabbing.

The results from the three different cycling profiles (TC, RTC, and TS) were fit to the data assuming a power law relationship between the number of cycles to failure and the profile cycle frequency, Figure 30. A stronger profile frequency dependence was seen for the SH and FC test structures as compared to the EI test structure. The FC structure has a lower variability due to coupon level IV measurements which aggregate the interconnections over a full coupon as opposed to measuring the resistance of each interconnect.

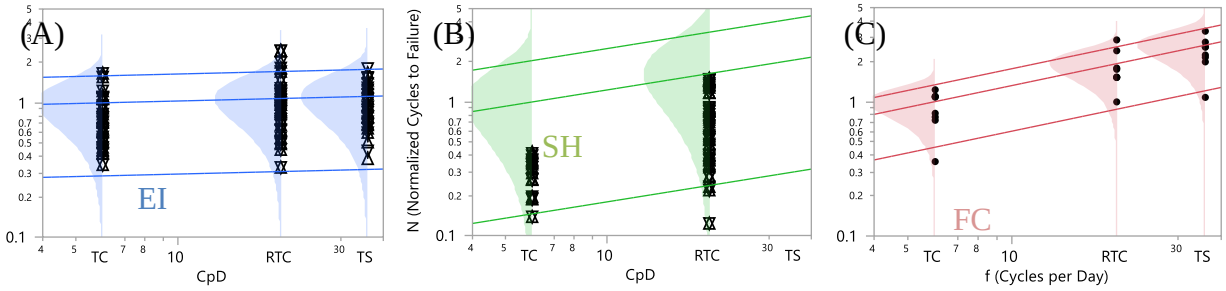

Figure 30. Cumulative probability distribution vs the number of cycles per day. Standard thermal cycling (TC) at 6 cycles per day. Rapid thermal cycling (RTC) at 20 cycles per day. And Thermal Shock (TC) at 36 cycles per day (A) Engineered interconnect test structures. (B) Shingled test structures (C) Front Contact test structures.[45]

Because the project did not get all the funding that was initially earmarked for this project, we did not get a chance to compare these indoor accelerated stress tests to outdoor tests on these test structures.

The work funded through this project was disseminated and published through conference presentations and peer reviewed publications including:

1. Michael Kempe, Peter Hacke, Joshua Morse, Jichao Li, Yu-Chen Shen, Katherine Han, “Electrochemical Mechanisms of Leakage-Current in Photovoltaic Modules”, Progress in Photovoltaics: Research and Applications. February 2023, https://dx.doi.org/10.1002/pip.3677
2. Michael D Kempe, Peter Hacke, Jichao Li, Katherine Han, Yu-Chen Shen, Staffan Westerberg, “Using Module Leakage Current Modeling to Understand Corrosion Chemistry”, WCPEC, Kona, Hawaii (2018).
3. Jichao Li, Yu-Chen Shen, Peter Hacke, Michael Kempe, “Electrochemical mechanisms of Leakage-current-enhanced delamination and corrosion in Si Photovoltaic modules”, Solar Energy Materials and Solar Cells 188, 273-279 (2018).
4. Peter Hacke, Jichao Li, Michael Kempe, Yu-Chen Shen, John Wohlgemuth, “Potential-Induced Degradation-Delamination Mode in Crystalline Silicon Modules”, Workshop on Crystalline Silicon Solar Cells and Modules: Materials and Processes, Vail, Colorado, August 28-31, 2016.

Subject Inventions Listing:

None.

ROI #:

None.

Bibliography

[1] C. R. Osterwald and T. J. McMahon, "History of accelerated and qualification testing of terrestrial photovoltaic modules: a literature review," *Prog. Photovolt: Res. Appl.,* vol. 17, pp. 11-33, 2009.

[2] A. M. Ricaud and R. C. Petersen, "Environmental stress tests: acceleration of corrosion," in *Proceedings of the 8th European Commission PV Solar Energy Conference*, Florence, Italy, 1988, pp. 549-553.

[3] M. D. Kempe, P. Hacke, J. Li, K. Han, Y. Shen, and S. Westerberg, "Using Module Leakage Current Modeling to Understand Corrosion Chemistry," in *2018 IEEE 7th World Conference on Photovoltaic Energy Conversion (WCPEC) (A Joint Conference of 45th IEEE PVSC, 28th PVSEC & 34th EU PVSEC)*, 2018, pp. 3558-3563.

[4] J. Li, Y.-C. Shen, P. Hacke, and M. Kempe, "Electrochemical mechanisms of leakage-current-enhanced delamination and corrosion in Si photovoltaic modules," *Solar Energy Materials and Solar Cells,* vol. 188, pp. 273-279, 2018/12/15/ 2018.

[5] M. Kempe, P. Hacke, J. Morse, J. Li, Y.-C. Shen, and K. Han, "Electrochemical mechanisms of leakage-current in photovoltaic modules," *Progress in Photovoltaics: Research and Applications,* vol. 31, no. 7, pp. 700-715, 2023.

[6] E. McCafferty, "Introduction to Corrosion Science," SpringerLink, Ed., ed: Springer Science+Business Media, LLC, 2010.

[7] M. D. Kempe, "Modeling of rates of moisture ingress into photovoltaic modules," *Solar Energy Materials and Solar Cells,* vol. 90, no. 16, pp. 2720-2738, 2006.

[8] J. Wohlgemuth, P. Hacke, N. Bosco, D. C. Miller, M. D. Kempe, and S. Kurtz, "Assessing the causes of delamination in PV modules," *43rd IEEE PVSC*, 2016.

[9] M. Pourbaix, "Atlas of electrochemical equilibria in aqueous solutions," 2d English ed. ed. Houston, Tex. :: National Association of Corrosion Engineers, 1974.

[10] J. Tracy, N. Bosco, and R. Dauskardt, "Encapsulant Adhesion to Surface Metallization on Photovoltaic Cells," *IEEE Journal of Photovoltaics*, vol. 7, no. 6, pp. 1635-1639, 2017.

[11] N. Bosco, P. Hacke, S. Kurtz, L. Tracy, and R. Dauskardt, "Adhesion Degradation of the Metallization-Encapsulant Interface," *EU PVSEC conference proceedings, Amsterdam, NL*, 2017.

[12] N. G. Dhere and N. R. Raravikar, "Adhesional shear strength and surface analysis of a PV module deployed in harsh coastal climate," *Solar Energy Materials and Solar Cells,* vol. 67, no. 1-4, pp. 363-367, 2001.

[13] J. Li, K. Han, Y.-C. Shen, S. Westerberg, M. D. Kempe, and P. L. Hacke, *Using Module Leakage Current Modeling to Understand Corrosion Chemistry* (Conference: Presented at the 2018 IEEE 7th World Conference on Photovoltaic Energy Conversion (WCPEC), 10-15 June 2018, Waikoloa Village, Hawaii). Piscataway, NJ: Institute of Electrical and Electronics Engineers (IEEE); National Renewable Energy Lab. (NREL), Golden, CO (United States), 2018, p. Medium: X.

[14] R. W. Warfield and M. C. Petree, "Electrical Resistivity of Polymers," *SPE Transactions,* 1961.

[15] A. Daire, "Improving the Repeatability of Ultra-High Resistance and Resistivity Measurements," *Keithley Instruments, Inc., Instruments Business Unit*.

[16] V. Naumann, K. K. Ilse, M. Pander, J. Tröndle, K. Sporleder, and C. Hagendorf, "Influence of soiling and moisture ingress on long term PID susceptibility of photovoltaic modules," *15th International Conference on Concentrator Photovoltaic Systems (CPV-15)*, 2019.

[17] J. D. Berghold, S. Koch, B. Frohmann, P. Hacke, and P. Grunow, "Properties of encapsulation materials and their relevance for recent field failures," *2014 IEEE 40th Photovoltaic Specialist Conference (PVSC)*, pp. 1987-1992, 2014.

[18] O. Adan, H. Huinink, N.J.W.Reuvers, and H. Fischer, *Plasticization of nylon-6 by water: a NMR imaging study*. 2013.

[19] M. D. Kempe and J. H. Wohlgemuth, "Evaluation of Temperature and Humidity on PV Module Component Degradation," in *39th IEEE PVSC*, Tampa, Florida, 2013.

[20] P. Hacke *et al.*, "System voltage potential-induced degradation mechanisms in PV modules and methods for test," in *Photovoltaic Specialists Conference (PVSC), 2011 37th IEEE*, 2011, pp. 000814-000820.

[21] P. Hacke, S. Johnston, W. Luo, S. Spataru, R. Smith, and I. Repins, "Prediction of Potential-Induced Degradation Rate of Thin-Film Modules in the Field Based on Coulombs Transferred," in *2018 IEEE 7th World Conference on Photovoltaic Energy Conversion (WCPEC) (A Joint Conference of 45th IEEE PVSC, 28th PVSEC & 34th EU PVSEC)*, 2018, pp. 3801-3806.

[22] M. Owen-Bellini, P. Hacke, S. Spataru, D. Miller, and M. Kempe, Combined-Accelerated Stress Testing for Advanced Reliability Assessment of Photovoltaic Modules. 2018.

[23] X. Jin *et al.*, "Theoretical insight into leakage current of solar module under high system voltage," in *2020 47th IEEE Photovoltaic Specialists Conference (PVSC)*, 2020, pp. 0109-0112.

[24] R. Swanson et al., "The surface polarization effect in high-efficiency silicon solar cells," Proceedings 15th International Photovoltaic Science and Engineering Conference (PVSEC-15), Shanghai, China, 2005, 2005.

[25] V. Naumann *et al.*, "Explanation of potential-induced degradation of the shunting type by Na decoration of stacking faults in Si solar cells," *Solar Energy Materials and Solar Cells,* vol. 120, pp. 383-389, 2014/01/01/ 2014.

[26] D. Lausch *et al.*, "Sodium Outdiffusion from Stacking Faults as Root Cause for the Recovery Process of Potential-induced Degradation (PID)," *Energy Procedia,* vol. 55, pp. 486-493, 2014/01/01/ 2014.

[27] H. Nagel, A. Metz, and K. Wangemann, Crystalline Si Solar Cells and Modules Featuring Excellent Stability Against Potential-Induced Degradation. 2011, pp. 3107-3112.

[28] M. Kutzer et al., Towards a Root Cause Model for the Potential-Induced Degradation in Crystalline Silicon Photovoltaic Cells and Modules. 2013.

[29] G. R. Mon and R. G. Ross, "Electrochemical degradation of amorphous-silicon photovoltaic modules," in *Proceedings of the 18th IEEE PV Specialists Conference*, Las Vegas, Nevada, USA, 1985, pp. 1142-1149.

[30] G. R. Mon, "Electrochemical aging effects in photovoltaic modules," 1986, vol. 26, p. 629.

[31] G. R. Mon, J. Orehotsky, R. G. Ross, Jr., and G. Whitla, "Predicting electrochemical breakdown in terrestrial photovoltaic modules," Kissimmee, FL,, 1984, pp. 682-692: Ieee.

[32] A. Sinha *et al.*, "Understanding interfacial chemistry of positive bias high-voltage degradation in photovoltaic modules," *Solar Energy Materials and Solar Cells,* vol. 223, p. 110959, 2021/05/01/ 2021.

[33] C. G. Reid, S. ferrigan, I. Fidalgo, and J. T. Woods, "Contribution of PV encapsulant composition to reduction of potential induced degradation (PID) of crystalline silicon PV cells," *28th European Photovoltaic Solar Energy Conference and Exhibition,* 2013.

[34] W. Luo *et al.*, "Potential-induced degradation in photovoltaic modules: a critical review," *Energy & Environmental Science,* 10.1039/C6EE02271E vol. 10, no. 1, pp. 43-68, 2017.

[35] B. M. Habersberger and P. Hacke, "ILLUMINATION AND ENCAPSULANT RESISTIVITY ARE CRITICAL FACTORS IN POLARIZATION-TYPE POTENTIAL INDUCED DEGRADATION ON N-PERT CELLS," *EUPVSEC,* September 2020 2020.

[36] B. M. Habersberger, P. Hacke, and L. S. Madenjian, "Evaluation of the PID-s susceptibility of modules encapsulated in materials of varying resistivity," in *2018 IEEE 7th World Conference on Photovoltaic Energy Conversion (WCPEC) (A Joint Conference of 45th IEEE PVSC, 28th PVSEC & 34th EU PVSEC)*, 2018, pp. 3807-3809.

[37] F. V. Natrup, H. Bracht, S. Murugavel, and B. Roling, "Cation diffusion and ionic conductivity in soda-lime silicate glasses," *Physical Chemistry Chemical Physics*, 10.1039/B502501J vol. 7, no. 11, pp. 2279-2286, 2005.

[38] P. Hacke *et al.*, "Testing and analysis for lifetime prediction of crystalline silicon PV modules undergoing degradation by system voltage stress," in *Photovoltaic Specialists Conference (PVSC), 2012 38th IEEE*, 2012, pp. 001750-001755.

[39] P. Hacke *et al.*, "Test-to-Failure of crystalline silicon modules," in *2010 35th IEEE Photovoltaic Specialists Conference*, 2010, pp. 000244-000250.

[40] J. Cueto and S. Rummel, "Degradation of Photovoltaic Modules Under High Voltage Stress in the Field: Preprint," *Proceedings of SPIE - The International Society for Optical Engineering*, vol. 7773, 08/01 2010.

[41] J. A. del Cueto and T. J. McMahon, "Analysis of leakage currents in photovoltaic modules under high-voltage bias in the field," *Progress in Photovoltaics: Research and Applications*, https://doi.org/10.1002/pip.401 vol. 10, no. 1, pp. 15-28, 2002/01/01 2002.

[42] P. Hacke, R. Smith, S. Kurtz, D. Jordan, and J. Wohlgemuth, "Modeling Current Transfer from PV Modules Based on Meterological Data," *IEEE PVSC, Portland, OR*, 2016.

[43] W. M. Bartczak and J. Kroh, "Theoretical models for electron conduction in polymer systems—I. Macroscopic calculations of d.c. transient conductivity after pulse irradiation," *International Journal of Radiation Applications and Instrumentation. Part C. Radiation Physics and Chemistry*, vol. 40, no. 5, pp. 369-376, 1992/11/01/ 1992.

[44] N. Saidi-Amroun, S. Berdous, M. Saidi, and M. Bendaoud, "Modeling of Transient Currents in Polyethylene Terephtalate," *International Journal of Polymer Analysis and Characterization*, vol. 12, no. 5, pp. 359-371, 2007/10/01 2007.

[45]J. Lippiatt, S. Westerberg, and D. Rose, "The Impact of a Faster Thermal Cycling Profile on PV Cell Interconnect Cycles to Failure," in *2018 IEEE 7th World Conference on Photovoltaic Energy Conversion (WCPEC) (A Joint Conference of 45th IEEE PVSC, 28th PVSEC & 34th EU PVSEC)*, 10-15 June 2018 2018, pp. 3819-3824, doi: 10.1109/PVSC.2018.8548099.